

Improving ASCAT Soil Moisture Retrievals With an Enhanced Spatially Variable Vegetation Parameterization

Hahn, Sebastian; Wagner, Wolfgang; Steele-Dunne, Susan C.; Vreugdenhil, Mariette; Melzer, Thomas

DOI

[10.1109/TGRS.2020.3041340](https://doi.org/10.1109/TGRS.2020.3041340)

Publication date

2020

Document Version

Final published version

Published in

IEEE Transactions on Geoscience and Remote Sensing

Citation (APA)

Hahn, S., Wagner, W., Steele-Dunne, S. C., Vreugdenhil, M., & Melzer, T. (2020). Improving ASCAT Soil Moisture Retrievals With an Enhanced Spatially Variable Vegetation Parameterization. *IEEE Transactions on Geoscience and Remote Sensing*, 59(10), 8241-8256. <https://doi.org/10.1109/TGRS.2020.3041340>

Important note

To cite this publication, please use the final published version (if applicable). Please check the document version above.

Copyright

Other than for strictly personal use, it is not permitted to download, forward or distribute the text or part of it, without the consent of the author(s) and/or copyright holder(s), unless the work is under an open content license such as Creative Commons.

Takedown policy

Please contact us and provide details if you believe this document breaches copyrights. We will remove access to the work immediately and investigate your claim.

Improving ASCAT Soil Moisture Retrievals With an Enhanced Spatially Variable Vegetation Parameterization

Sebastian Hahn¹, Wolfgang Wagner¹, *Senior Member, IEEE*, Susan C. Steele-Dunne², *Member, IEEE*, Mariette Vreugdenhil¹, *Member, IEEE*, and Thomas Melzer

Abstract—This study investigates the performance of the TU Wien soil moisture retrieval (TUW-SMR) algorithm by adapting the strength of the vegetation correction. The semiempirical change detection method TUW-SMR exploits the multiangle backscatter observations from spaceborne fan-beam scatterometer systems in order to derive surface soil moisture information expressed in the degree of saturation. The vegetation parameterization of TUW-SMR is controlled by the dry and wet crossover angles that are used to determine the dry and wet backscatter reference. Backscatter observations from the Advanced Scatterometer (ASCAT) are used to produce four soil moisture data sets based on different dry and wet crossover angles describing: 1) a static, respectively, no vegetation correction; 2) the currently used seasonal vegetation correction; 3) a stronger seasonal vegetation correction; and 4) a spatially variable seasonal vegetation correction with the stronger vegetation correction over vegetated areas and no vegetation correction over bare land. All four ASCAT soil moisture data sets are evaluated against soil moisture estimates from GLDAS-2.1 Noah land surface model and the European Space Agency (ESA) climate change initiative (CCI) Passive v04.5 soil moisture product using the triple collocation method and traditional correlation analysis. The results show that the spatially variable vegetation correction overall improves soil moisture estimates in both more densely vegetated areas, e.g., in large parts of North America and Europe, and more sparsely vegetated, e.g., Western Africa. Nonetheless, the experiment also provides insight into challenging retrieval conditions where the TUW-SMR fails to take all relevant backscatter processes into account, e.g., wetlands and bare soils with subsurface scattering.

Index Terms—Performance evaluation, radar cross sections, radar remote sensing, soil moisture.

I. INTRODUCTION

THE topic of microwave remote sensing of soil moisture has been studied extensively [1]–[4]. Microwaves exhibit

Manuscript received July 6, 2020; revised October 16, 2020; accepted November 21, 2020. Date of publication December 21, 2020; date of current version September 27, 2021. This work was supported in part by the European Organisation for the Exploitation of Meteorological Satellites (EUMETSAT) Satellite Application Facility on Support to Operational Hydrology and Water Management (H SAF), in part by the Austrian Space Application Program through the BMon under Grant 872408, and in part by the Daily Water Cycle (DWC) -Radar Projects under Grant 873658. (*Corresponding author: Sebastian Hahn.*)

Sebastian Hahn, Wolfgang Wagner, Mariette Vreugdenhil, and Thomas Melzer are with the Department of Geodesy and Geoinformation, Vienna University of Technology (TU Vienna), 1040 Vienna, Austria (e-mail: sebastian.hahn@geo.tuwien.ac.at; wolfgang.wagner@geo.tuwien.ac.at; mariette.vreugdenhil@geo.tuwien.ac.at; thomas.melzer@geo.tuwien.ac.at).

Susan C. Steele-Dunne is with the Faculty of Civil Engineering and Geosciences, Delft University of Technology, 2628 Delft, The Netherlands (e-mail: s.c.steele-dunne@tudelft.nl).

Digital Object Identifier 10.1109/TGRS.2020.3041340

1558-0644 © 2020 IEEE. Personal use is permitted, but republication/redistribution requires IEEE permission.

See <https://www.ieee.org/publications/rights/index.html> for more information.

a strong dependence on the soil dielectric properties, which are largely controlled by the water content in the soil. In addition, microwaves benefit from the fact that they are hardly affected by clouds and independent of solar illumination. Therefore, microwaves have proven to be a useful tool to measure soil moisture changes over land.

Numerous satellite soil moisture products have been developed and published based on active and passive microwave instruments [5]–[11]. Furthermore, an effort has been directed toward merging active and passive microwave satellite soil moisture products in the framework of European Space Agency (ESA's) climate change initiative (CCI) [12], [13]. By harnessing the assets of active and passive microwave instruments, it is possible to overcome the limitations of one technique by another.

However, vegetation cover effects are still a challenge when deriving surface soil moisture information from active and passive microwave instruments. When the soil surface is covered by vegetation, part of the microwave radiation is absorbed and scattered. A mix of surface, volume, and multiple scattering is reducing the signal sensitivity to soil moisture [14], [15]. Various approaches have been investigated to account for vegetation effects e.g., using optical vegetation indices [e.g., Normalized Difference Vegetation Index (NDVI), Leaf Area Index (LAI)] [16], [17], directly estimating vegetation parameters from microwave measurements (e.g., Vegetation Optical Depth (VOD), Radar Vegetation Index (RVI), polarization ratio) [4], [9], [18], or exploiting multiangle backscatter observations [10], [19]. The TU Wien soil moisture retrieval (TUW-SMR) algorithm belongs to the last category, since it utilizes the multiangle measurement capabilities of spaceborne fan-beam scatterometer to account for vegetation during the retrieval of surface soil moisture [20].

TUW-SMR was originally developed for the C-band scatterometer instruments onboard European Remote-Sensing Satellite (ERS)-1 and ERS-2 [10] and later applied to the Advanced Scatterometer (ASCAT) on-board the series of Metop satellites [11], [21]. The vegetation parameterization of TUW-SMR exploits the incidence angle dependence of backscatter, relating it to vegetation and soil-vegetation interaction effects [22], [23]. It is based on the assumption that a change in soil moisture equally affects the backscatter intensity (expressed in dB) across the incidence angle range between 20°–60°, whereas vegetation phenology results in more complex variations in the incidence angle dependence of backscatter. Applying this abstraction to specific soil and

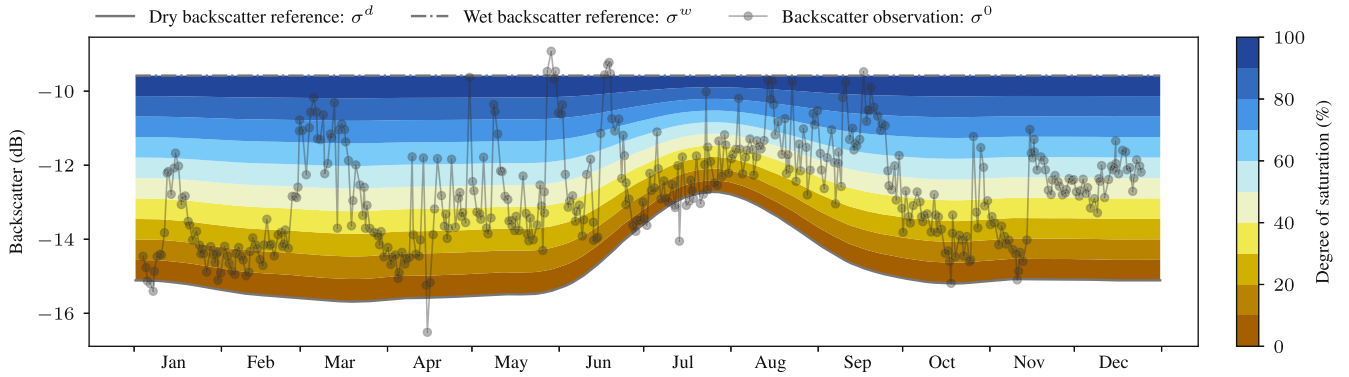


Fig. 1. TUV-SMR is a physically based semiempirical change detection method. Backscatter observations σ^0 are normalized to a common reference incidence angle ($\theta_r = 40^\circ$) and scaled between a dry and wet backscatter reference (σ^d , σ^w). Soil moisture is expressed in degree of saturation ranging between 0 (dry soil conditions) and 100% (saturated soil condition).

vegetation states eventually leads to intersections at certain incidence angles. The so-called crossover angle concept utilizes this behavior by defining two distinct incidence angle at which the backscatter signal is independent of vegetation changes in the case of dry and wet (saturated) soil. Based on empirical observations from previous studies using ERS-1 and ERS-2 scatterometer data, the dry and wet crossover angles are set to $\theta_d = 25^\circ$ and $\theta_w = 40^\circ$ globally [10], [22], [24]. The choice of the crossover angles is important because they directly influence the amplitude of the dynamic vegetation correction and ultimately determine the signal sensitivity to soil moisture (i.e., the distance between the dry and wet backscatter reference).

Recent research has shown that in some areas seasonal vegetation biases are evident [25], [26]. The selection of θ_d and θ_w has not been changed since the initial development of TUV-SMR and no dedicated experiments have so far been conducted changing them on a global scale. A first study adapting the vegetation parameterization to regional conditions indicated a clear benefit of using a stronger vegetation correction in an agricultural area in Lower Austria [27].

In the present study, we evaluate the performance of TUV-SMR globally using different pairs of dry and wet crossover angles:

- 1) $\theta_d = 40^\circ$ and $\theta_w = 40^\circ$ which switches off the vegetation correction over bare land surface areas, respectively, assumes that the scattering behavior of vegetation is stable over the year.
- 2) $\theta_d = 25^\circ$ and $\theta_w = 40^\circ$ representing the current seasonal vegetation correction.
- 3) $\theta_d = 10^\circ$ and $\theta_w = 30^\circ$ representing the stronger vegetation parameterization successfully tested by [27] over temperate climates.
- 4) a spatially variable choice of crossover angles derived from a Vegetation Continuous Fields (VCF) data set to tune the vegetation correction from no vegetation correction over bare land surfaces to the stronger vegetation parameterization over vegetated areas.

Hence, four different ASCAT surface soil moisture data records are computed and evaluated using soil moisture information from the Global Land Data Assimilation

System (GLDAS) Noah v2.1 [28] and the ESA CCI Passive soil moisture data set v4.5 [29] for the time period January 2007 until December 2018. The main performance metrics computed in this study are the Pearson correlation coefficient and the estimated error variance expressed as signal-to-noise ratio (SNR) derived using triple collocation (TC) [30], [31].

II. BACKGROUND

A. TUV-SMR Algorithm

The TUV-SMR represents a change detection method developed for scatterometer instruments in 1999 [10], [22], [24]. Stepwise improvements have been developed in the past years, such as correcting azimuthal anisotropy [32], supporting Metop ASCAT [21] and error characterization [33]. Fig. 1 illustrates the final step in the change detection method and (1) its mathematical expression. Backscatter observations (σ^0) normalized to a common reference incidence angle ($\theta_r = 40^\circ$) are scaled between a dry and wet backscatter reference (σ^d , σ^w), resulting in relative surface soil moisture information (m_s) expressed in degree of saturation. The surface soil moisture values range between 0 (dry soil conditions) and 100% (saturated soil conditions) and any σ^0 observation outside the dry/wet backscatter reference are either corrected to 0/100% or rejected as an extreme outlier

$$m_s(t) = \frac{\sigma^0(t) - \sigma^d(t)}{\sigma^w(t) - \sigma^d(t)} \cdot 100 \quad [\%]. \quad (1)$$

The physical basis of TUV-SMR can be attributed to the strong linear relationship between C-band backscatter and soil water content in the top soil layer (1–2 cm) [11]. Despite the lack of a direct parameterization of common soil surface properties (e.g., surface roughness, vegetation, and land cover) which are usually part of semiempirical or theoretical backscatter models, TUV-SMR is grounded on physical principles and the following basic assumptions [10]:

- 1) The relationship between the backscatter coefficient σ^0 expressed in decibels (dB) and the surface soil moisture content is linear.
- 2) Surface roughness and land cover are temporally stable at a spatial resolution of 25/50 km.

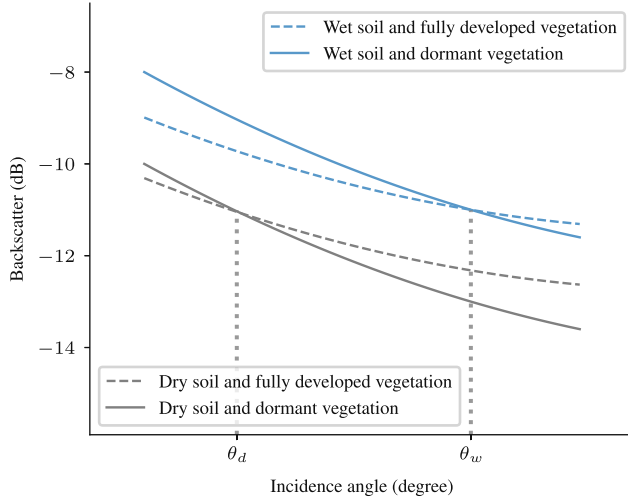


Fig. 2. Illustration of the crossover angle concept after [24]. Two distinct intersections can be registered for dry and wet soil conditions, which are called dry and wet crossover angles (θ_d , θ_w).

- 3) The incidence angle dependence of σ^0 characterizes soil roughness conditions and land cover dynamics, but is not affected by changes in the surface soil moisture content.
- 4) The effect of vegetation on σ^0 changes on a seasonal scale without interannual variations.

One advantage of this method is that model parameterization is possible without an iterative adjustment, which is normally necessary for more complex backscatter models. Furthermore, the simple mathematical description allows for a straightforward application of error propagation analysis to estimate a retrieval error of the final surface soil moisture estimate [23].

TUW-SMR model parameters can either be predefined globally or estimated for each individual location on the land surface. Thus, model parameters can be spatially and temporally constant (i.e., $\theta_r = 40^\circ$, $\theta_d = 25^\circ$, $\theta_w = 40^\circ$) or change temporally and geographically (i.e., σ' , σ'' , σ^d , σ^w). The estimation of the unknown model parameters is typically done in the time domain and computationally expensive. Long-term backscatter time series (>2–4 years) are needed for each location in order to compute robust results.

B. Crossover Angle Concept

TUW-SMR assumes that distinct crossover angles exist at which the backscatter signal is independent of vegetation phenology. Fig. 2 depicts this concept showing backscatter curves for four special cases. Two distinct intersections can be registered, the so-called dry and wet crossover angles (θ_d , θ_w), where backscatter intensity is no longer dependent on the vegetation state. The selection of $\theta_d = 25^\circ$ and $\theta_w = 40^\circ$ is based on empirical observations and analysis from previous studies [10], [22], [24].

The dry and wet crossover angles are important parameters because the dry and wet backscatter references are computed at these incidence angles. A second-order Taylor polynomial is used to describe the incidence angle dependence of backscatter (see (2)). The so-called slope σ' and curvature σ'' are used to

normalize backscatter observed at arbitrary incidence angles (σ_θ^0) to a common reference incidence angle ($\theta_r = 40^\circ$). σ' and σ'' represent the first and second derivatives of backscatter with respect to the incidence angle, which are estimated for each location independently and change temporally [34]

$$\sigma^0(t) = \sigma_\theta^0(t) - \sigma'(t) \cdot (\theta - \theta_r) - \frac{1}{2} \cdot \sigma''(t) \cdot (\theta - \theta_r)^2. \quad (2)$$

Rearranging (2) allows us to convert σ^0 from the reference incidence angle θ_r to θ_d and θ_w , respectively

$$\sigma_d^0(t) = \sigma^0(t) + \sigma'(t) \cdot (\theta_d - \theta_r) + \frac{1}{2} \cdot \sigma''(t) \cdot (\theta_d - \theta_r)^2 \quad (3)$$

$$\sigma_w^0(t) = \sigma^0(t) + \sigma'(t) \cdot (\theta_w - \theta_r) + \frac{1}{2} \cdot \sigma''(t) \cdot (\theta_w - \theta_r)^2 \quad (4)$$

The backscatter time series at the crossover angle (σ_d^0 , σ_w^0) are used to determine the dry and wet backscatter reference from the extreme lowest and highest backscatter values. The selection of the extreme backscatter observations is based on a confidence interval determined by the noise distribution of the backscatter at the respective crossover angle [23]. The average of the two selected backscatter subsamples represents the dry and wet backscatter reference at the dry and wet crossover angles (C_d^0 , C_w^0). A final transformation of C_d^0 and C_w^0 is needed in order to convert the backscatter values from the crossover angles back to $\theta_r = 40^\circ$

$$\sigma^d(t) = C_d^0 - \sigma'(t) \cdot (\theta_d - \theta_r) - \frac{1}{2} \cdot \sigma''(t) \cdot (\theta_d - \theta_r)^2 \quad (5)$$

$$\sigma^w(t) = C_w^0 - \sigma'(t) \cdot (\theta_w - \theta_r) - \frac{1}{2} \cdot \sigma''(t) \cdot (\theta_w - \theta_r)^2. \quad (6)$$

It is worth noting that C_d^0 and C_w^0 are both constant values (at the respective crossover angle), but as a result of the final transformation to θ_r , σ' and σ'' impose their temporal signature on σ^d and σ^w . Technically, this is only the case for σ^d for the current settings, because $\theta_r = \theta_w$.

Fig. 3 shows an example of σ^d and σ^w determined at different crossover angles and transformed back to θ_r . It can be seen that the selection of the crossover angle controls the strength of the temporal characteristics. A lower crossover angle enhances the temporal signature coming from σ' and σ'' . In the extreme case that the crossover angle is equal to the reference incidence angle, no transformation is necessary and the reference is constant. The distance between σ^d and σ^w determines the backscatter signal sensitivity to changes in soil moisture. Naturally, with increasing vegetation coverage, backscatter sensitivity to changes in soil moisture is decreasing due to attenuation effects. A typical variable in microwave remote sensing describing vegetation attenuation properties is the VOD. In fact, [20] developed a method deriving VOD by ingesting σ^d and σ^w into a water cloud model (WCM) [14], [35], which compared well in temperate and continental climates to VOD derived from passive microwave observations. Hence, the selection of θ_d and θ_w determines the temporal development of σ^d and σ^w , which, ultimately, can be interpreted as changes in VOD.

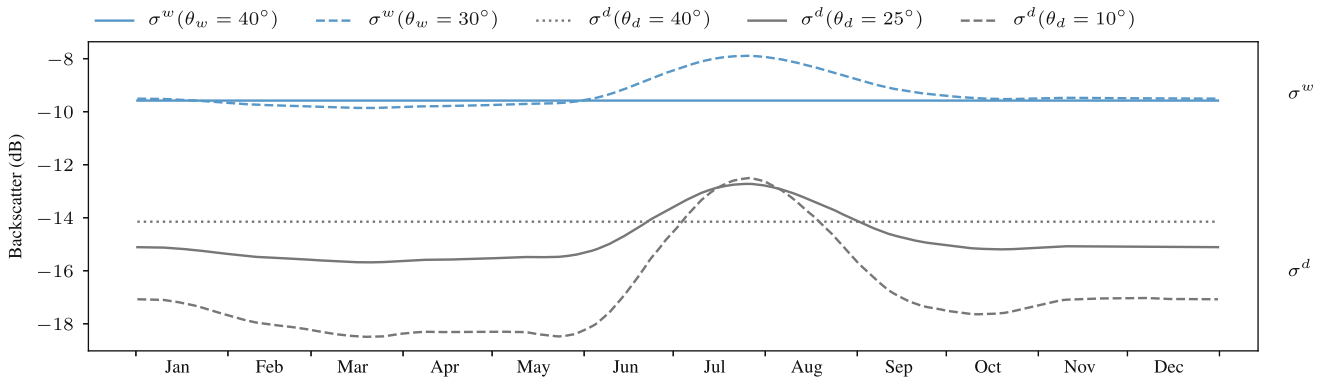


Fig. 3. Examples of different dry (σ^d) and wet (σ^w) backscatter references at $\theta_r = 40^\circ$ derived using different dry and wet crossover angles ($\theta_d = \{10^\circ, 25^\circ, 40^\circ\}$, $\theta_w = \{30^\circ, 40^\circ\}$).

III. DATA SETS

A. Metop ASCAT Backscatter

The ASCAT on-board the series of Metop satellites is an active C-band (5.255 GHz) radar using six vertically polarized fan-beam antennas. From around 800 km altitude ASCAT transmits well-characterized pulses of microwave energy toward the Earth's surface and measures the reflected energy expressed in terms of the normalized radar cross section (NRCS), also known as backscatter coefficient σ^0 [36]. ASCAT represents a follow-on scatterometer for the Active Microwave Instruments (AMI) on-board ERS-1 and ERS-2 [37] and has proven to be a stable and well-calibrated instrument [38], [39]. Two main Level 1b backscatter products are generated by spatially averaging the geolocated full resolution backscatter measurements in order to obtain σ^0 triplets from the fore, mid, and aft beam resampled on a regular orbit grid: Sigma Zero Operational (SZO) with a spatial resolution of about 50 km, sampled on 21 nodes across each swath, with a spacing of approximately 25 km between nodes and successive rows of nodes and Sigma Zero Research (SZR) with a spatial resolution of 25–34 km, sampled on 41 nodes across each swath, with a spacing of approximately 12.5 km [39]. The latter uses a dynamic filter size in order to maintain a similar radiometric resolution at the cost of altering the spatial resolution in the cross-track direction.

At the moment, all three Metop satellites share the same sun-synchronous orbit and each carries an ASCAT instrument. The series of Metop satellites was launched 6 years apart, starting with Metop-A in October 2006, Metop-B in September 2012, and Metop-C in November 2018. In order to extend the lifetime of Metop-A, the spacecraft will be directed into a drifting orbit shifting the satellites Local Time of the Descending Node (LTDN) from 9:30 a.m. (nominal) to 7:30 a.m. by April 2022. Afterward, Metop-A will be deorbited into a 25 years reentry orbit [40].

In this study, we used Metop-A and Metop-B Level 1b SZR products, which have been downloaded from the EUMETSAT data center.¹ In case of the Metop-A, a Fundamental Climate Data Record (FCDR) exists covering January 2007 to

March 2014, which has been extended with the Metop-A Level 1b SZR product from the operational ground segment until December 2018. Currently, no FCDR is available for Metop-B, therefore the Metop-B Level 1b SZR product from the operational ground segment has been downloaded for the period January 2013 until December 2018.

B. GLDAS-2.1 Noah Soil Moisture

The GLDAS is a global, high-resolution, offline (uncoupled to the atmosphere) terrestrial modeling system that ingests satellite- and ground-based observations and has been developed jointly by the National Aeronautics and Space Administration (NASA) Goddard Space Flight Center (GSFC) and the National Oceanic and Atmospheric Administration (NOAA) National Centers for Environmental Prediction (NCEP) [28], [41]. In this article, we used the GLDAS-2.1 Noah 0.25 degree 3-hourly product, which has been simulated with the Noah Model 3.3 in the Land Information System (LIS) version 7 [42]. It contains 36 land surface fields from January 2000 until the present. The data were downloaded from the NASA Goddard Earth Sciences Data and Information Services Center (GES DISC) for the period January 2007 until December 2018.²

The Noah model incorporates soil-vegetation-atmosphere transfer schemes (SVATS), with vegetation properties controlling fluxes and storages of energy and water at the land surface. GLDAS makes use of a vegetation classification map and also utilizes satellite-derived LAI from both the Advanced Very High Resolution Radiometer (AVHRR) and MODerate-resolution Imaging Spectroradiometer (MODIS) sensors (Rodell *et al.* 2004). Therefore, unlike active and passive microwave-based soil moisture products (where vegetation is part of the received signal and needs to be accounted for), the seasonal cycle of GLDAS soil moisture is indirectly affected by vegetation controlled by SVATS.

GLDAS-2.1 Noah has a total of four different layers representing soil moisture: 0–10 cm, 10–40 cm, 40–100 cm, and 100–200 cm expressed in kg m^{-2} . In this study, we used soil moisture information from the first soil layer 0–10 cm, as well as snow water equivalent (SWE) and soil temperature

¹<https://eportal.eumetsat.int/>

²<https://disc.gsfc.nasa.gov/>

0–10 cm to mask potentially invalid remote sensing soil moisture observations.

C. ESA CCI Passive Soil Moisture

In 2009, the ESA started the CCI in response to the need for climate-monitoring satellite data. Soil moisture has been recognized as an Essential Climate Variable (ECV) and became part of the ESA CCI program in 2012. The ESA CCI soil moisture project³ combines multiple active and passive microwave soil moisture products generating three harmonized climate data records: Active, Passive, and Merged. In this study, we used the ESA CCI Passive soil moisture product v04.5 expressing surface soil moisture in $m^3 m^{-3}$ covering the period from 1978-11-01 until 2018-12-31 [29], [43], [44].

The main data sources for the ESA CCI Passive product v04.5 for the period under investigation (2007–2018) are based on Advanced Microwave Scanning Radiometer (AMSR)-E, WindSat, AMSR2, and Soil Moisture and Ocean Salinity (SMOS). All satellite data are processed with the so-called Land Parameter Retrieval Model (LPRM) [45]. LPRM is a zero-order radiative transfer model and makes use of the microwave polarization difference index (MPDI) to calculate VOD, which is used to parameterize the attenuation of the signal by the vegetation [46].

D. VCF-VCF5KYR

The NASA Making Earth System Data Records for Use in Research Environments (MEaSUREs)⁴ VCF Version 1 data product (VCF5KYR) provides global fractional vegetation cover at 0.05° spatial resolution at yearly intervals from 1982 to 2016 [47]. The VCF5KYR product is derived from a bagged linear model algorithm using observations from the AVHRR Long Term Data Record Version 4 (LTDR V4). The three bands included in VCF5KYR are: percent of tree cover (*tc*), nontree vegetation (*v*), and bare ground (*bg*).

In this study, we utilized the VCF5KYR 2016 data to estimate the dry ((7)) and wet ((8)) crossover angle. The three bands are used as weights assuming that no vegetation correction is required in case of bare ground ($\theta_d = \theta_w = 40^\circ$), while tree and nontree vegetated surfaces tend to have lower crossover angle ($\theta_d = 10^\circ, \theta_w = 30^\circ$)

$$\theta_d = 10 \cdot v + 10 \cdot tc + 40 \cdot bg \tag{7}$$

$$\theta_w = 30 \cdot v + 30 \cdot tc + 40 \cdot bg. \tag{8}$$

The global maps shown in Fig. 4 illustrate the spatial distribution of θ_d and θ_w derived from the VCF5KYR 2016 data set using (7) and (8).

E. Köppen–Geiger Climate Classification

The Köppen–Geiger climate classification⁵ realized by [48] is sampled on a regular 0.5° latitude/longitude grid and defines 30 climate classes (see Table I). In this study, we used the Köppen–Geiger classification to group validation results by climate type around the world.

³<http://www.esa-soilmoisture-cci.org/>

⁴<https://earthdata.nasa.gov/community/community-data-system-programs/measures-projects>

⁵<https://people.eng.unimelb.edu.au/mpeel/koppen.html>

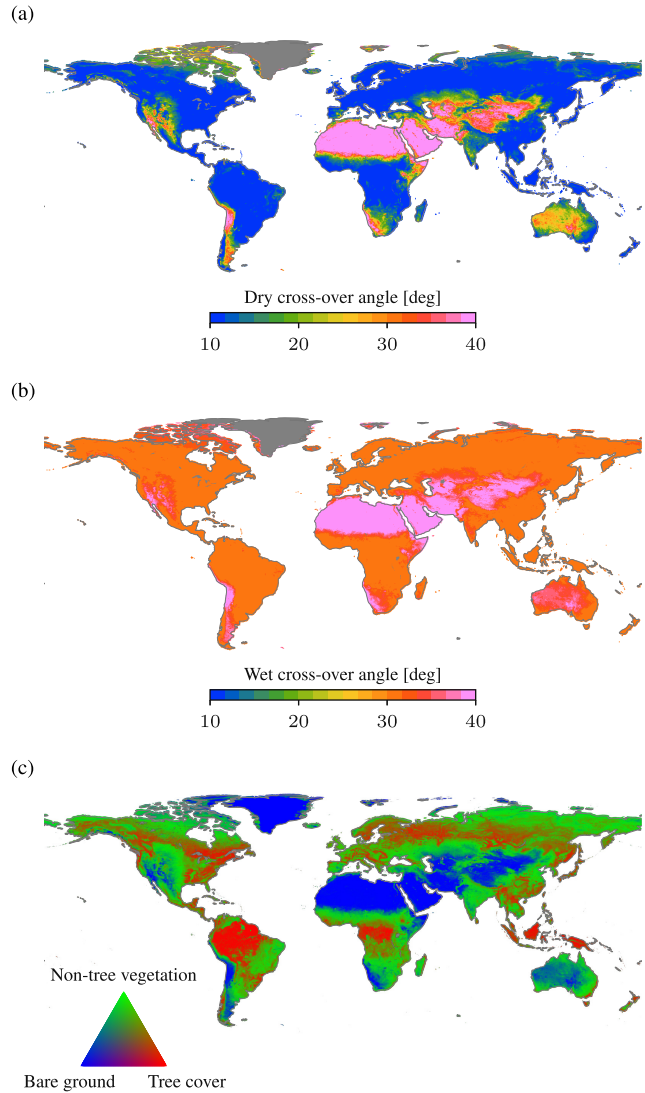


Fig. 4. Dry (a) and wet (b) crossover angles derived from the VCF5KYR 2016 data set (c).

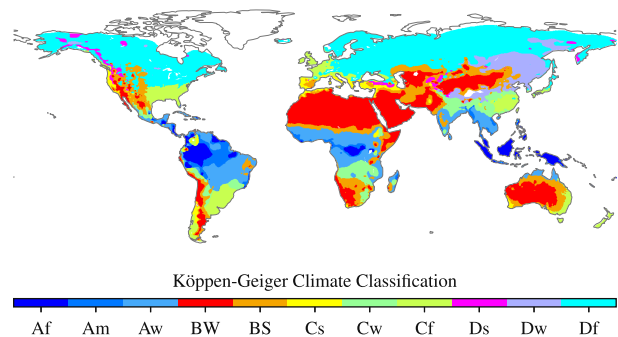


Fig. 5. Köppen Geiger climate classification map.

F. ESA CCI Land Cover

The ESA CCI Land Cover project provides annual land cover maps (1992–2015) at 300 m spatial resolution [49]. The land cover map 2015 v2.0.7 was aggregated to 12.5 km collecting the fractional area of each land cover class and its majority class. The data set was used to group validation results by land cover type. Subclasses are merged into their respective main class (see Table II).

TABLE I
KÖPPEN-GEIGER CLIMATE SYMBOLS AFTER [48]

1st	2nd	3rd	Description
A			Tropical
	f		- Rainforest
	m		- Savannah
B			Arid
	W		- Desert
	S		- Steppe
		h	- Hot
		k	- Cold
C			Temperate
	s		- Dry Summer
	w		- Dry Winter
	f		- Without dry season
		a	- Hot Summer
		b	- Warm Summer
		c	- Cold Summer
D			Cold
	s		- Dry Summer
	w		- Dry Winter
	f		- Without dry season
		a	- Hot Summer
		b	- Warm Summer
		c	- Cold Summer
		d	- Very Cold Winter
E			Polar
	T		- Tundra
	F		- Frost

TABLE II
ESA CCI LAND COVER CLASS DESCRIPTIONS

Identifier	Description
10, 11, 12	Cropland, rainfed
20	Cropland, irrigated or post-flooding
30	Mosaic cropland (>50%) / natural vegetation (tree, shrub, herbaceous cover)
40	Mosaic natural vegetation (tree, shrub, herbaceous cover) (>50%) / mosaic cropland
50	Tree cover, broadleaved, evergreen, closed to open (>15%)
60, 61, 62	Tree cover, broadleaved, deciduous, closed to open (>15%)
70, 71, 72	Tree cover, needleleaved, evergreen, closed to open (>15%)
80, 81, 82	Tree cover, needleleaved, deciduous, closed to open (>15%)
90	Tree cover, mixed leaf type
100	Mosaic tree and shrub (>50%), herbaceous cover (<50%)
110	Mosaic herbaceous cover (>50%), tree and shrub (<50%)
120, 121, 122	Shrubland
130	Grassland
140	Lichens and mosses
150, 151, 152, 153	Sparse vegetation (tree, shrub, herbaceous cover)
160, 170	Tree cover, flooded, saline, fresh or brakish water
180	Shrub or herbaceous cover, flooded, fresh/saline/brakish water
200, 201, 202	Bare areas

IV. METHODS

TUW-SMR was applied to Metop-A and Metop-B ASCAT backscatter observations, which were resampled from their original orbit swath geometry to a fixed Earth grid beforehand. This preprocessing step is necessary because backscatter observations in time series format are needed by TUW-SMR.

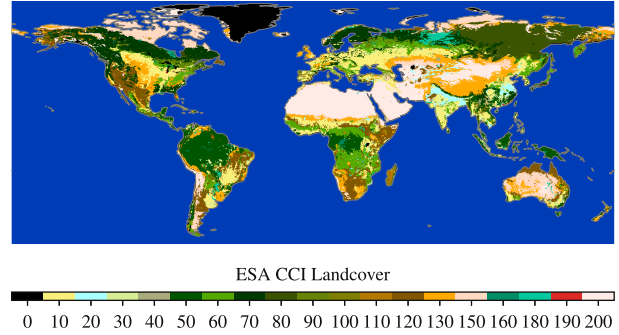


Fig. 6. ESA CCI land cover map 2015 (v2.0.7).

TABLE III
ASCAT SOIL MOISTURE DATA SETS

Name	θ_d [°]	θ_w [°]	Description
ASCAT SM-10/30	10	30	strong vegetation correction
ASCAT SM-25/40	25	40	present standard settings
ASCAT SM-40/40	40	40	only static vegetation correction
ASCAT SM-Dyn	10-40	30-40	variable cross-over angles

The so-called WARP5 grid was used as a spatial reference with a global equidistant sampling of 12.5 km [23]. A search radius of 34 km was centered around each WARP5 land grid point selecting original orbit swath backscatter observations inside, which were subsequently weighted and averaged using a Hamming window function. In this way, a backscatter time series was generated incrementally and used as input for TUW-SMR. TUW-SMR was applied four times, with each run generating a surface soil moisture data set based on a different set of crossover angles (see Table III).

The ASCAT surface soil moisture data sets (ASCAT SM-10/30, ASCAT SM-25/40, ASCAT SM-40/40, and ASCAT SM-Dyn) were validated against GLDAS-2.1 Noah and CCI Passive soil moisture computing the Pearson correlation coefficient (R) and by applying TC. TC is a method to study error characteristics from three spatially and temporally collocated data sets [30]. The mean squared random error of all three data sets are estimated individually by cross-multiplying differences between them. The computed error variance can be expressed in absolute terms, but as shown in [31], the obtained noise variance can also be related to the signal variance leading to the SNR. SNR expressed in decibel (dB) allows for a physically meaningful interpretation: if signal and noise variance are equal, SNR is zero, whereas each doubling/halving of their ratio corresponds to additional ± 3 dB.

The temporal period under investigation was 2007-01-01 until 2018-12-31, which is covered by all soil moisture data sets. In order to calculate the validation metrics (R , SNR), spatial and temporal collocation has been performed. In the spatial domain, the WARP5 grid was used as a reference selecting nearest neighbors from the GLDAS-2.1 Noah and CCI Passive grid. In the temporal domain, the ASCAT soil moisture time stamps were used to find the closest corresponding soil moisture observation within ± 8 hours from GLDAS-2.1 Noah and CCI Passive. Time periods with frozen soil conditions and snow cover were masked out beforehand using soil temperature ($< 4^\circ$) and SWE (> 0) information provided by GLDAS-2.1 Noah. The temporal matching was performed

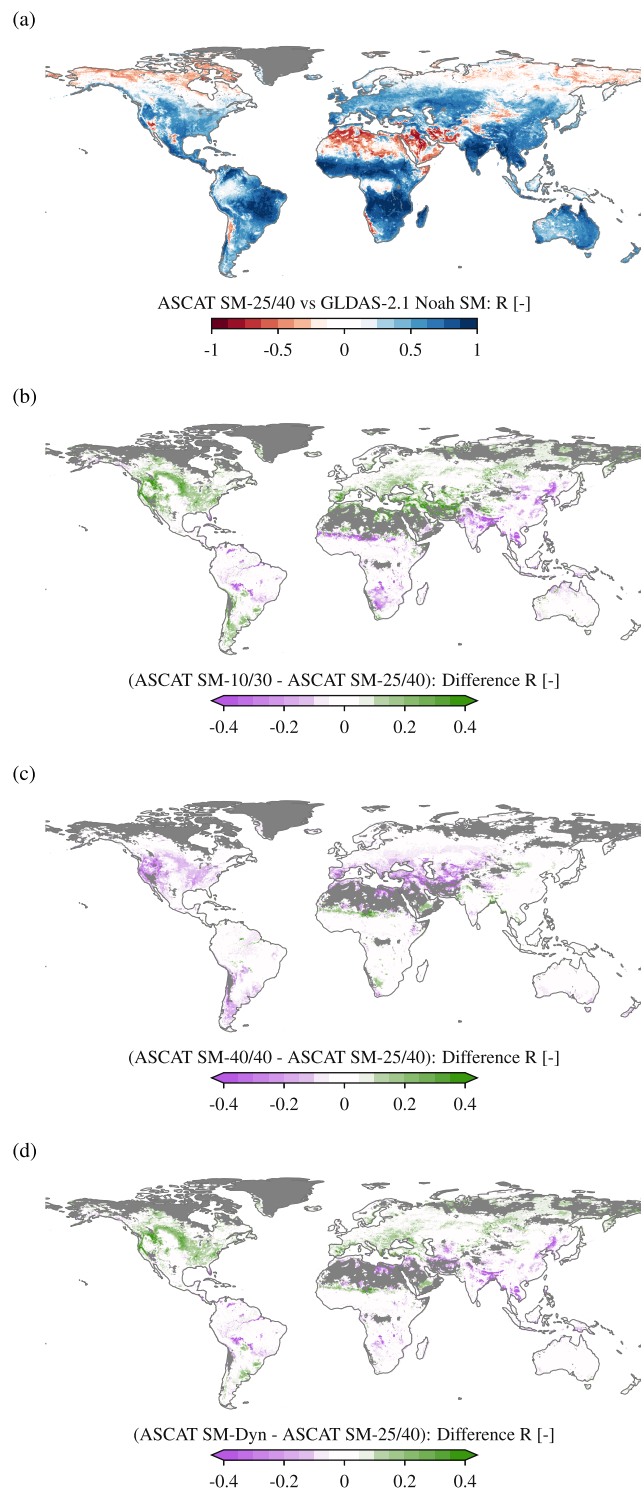


Fig. 7. Global maps of Pearson R ($p < 0.05$ and more than 100 observations). Difference between Pearson R is shown only if both Pearson R values are positive.

only between two data sets for the computation of Pearson R , while in the case of TC the temporal matching was carried out between all three data sets.

V. RESULTS AND DISCUSSION

A. Pearson R

Figs. 7 and 8 show the result of Pearson R for ASCAT SM-25/40 and the difference against the other ASCAT SM

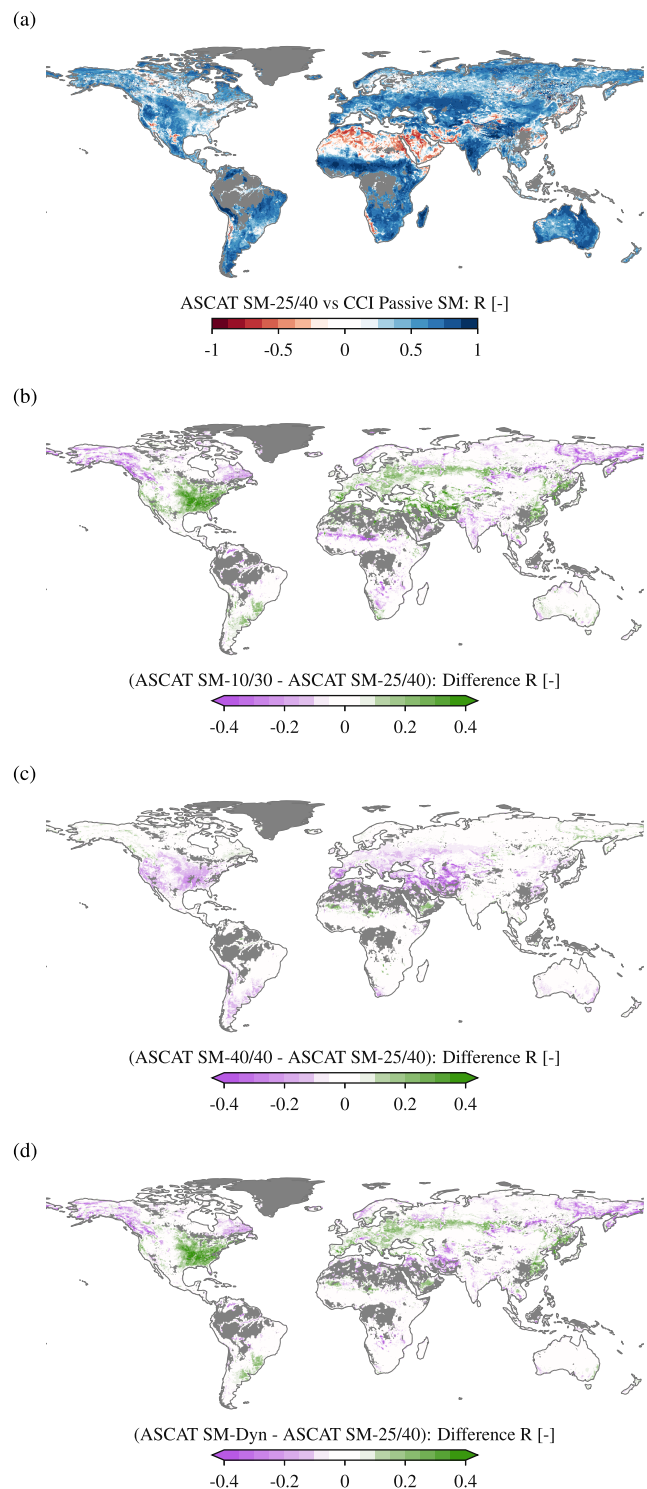


Fig. 8. Global maps of Pearson R ($p < 0.05$ and more than 100 observations). Difference between Pearson R is shown only if both Pearson R values are positive.

data sets. Locations with p -values < 0.05 are shown in Figs. 7(a) and 8(a), whereas the difference of Pearson R [Figs. 7(b)–(d) and 8(b)–(d)] is only shown in the case of positive correlations. Pearson R obtained from ASCAT SM-25/40 with good temporal correlations similar to Pearson R com-

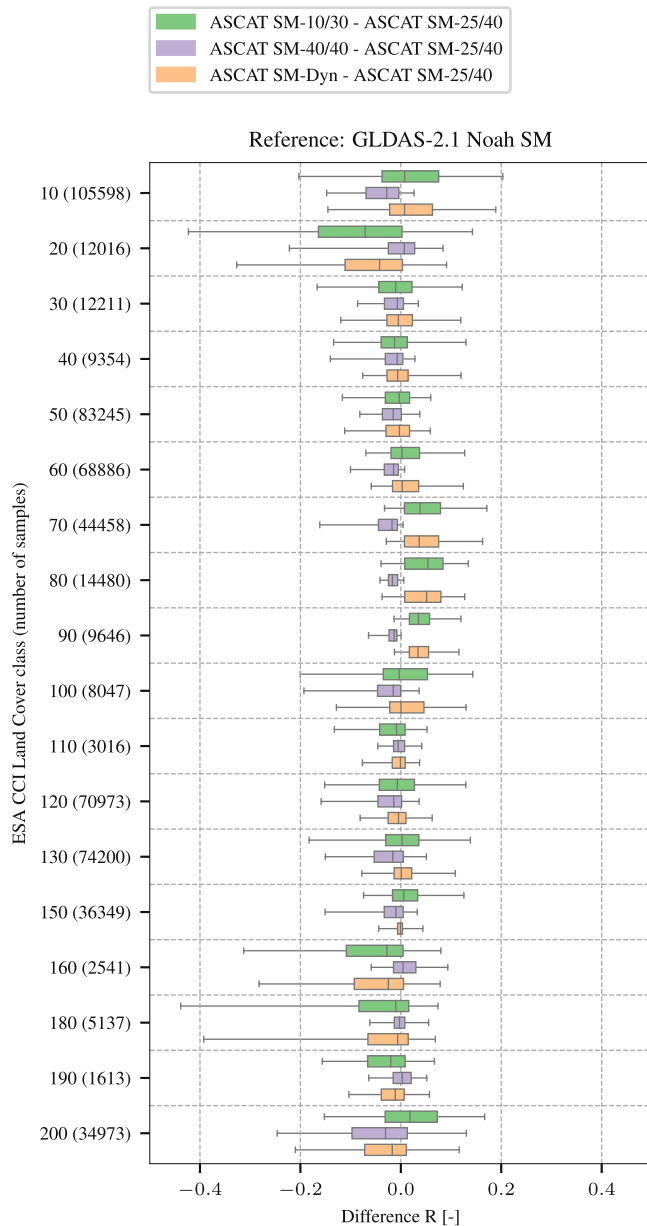


Fig. 9. Difference of Pearson R summarized as boxplot per land cover class using Noah GLDAS-2.1 SM as reference. Whisker ends represent 5th and 95th percentile.

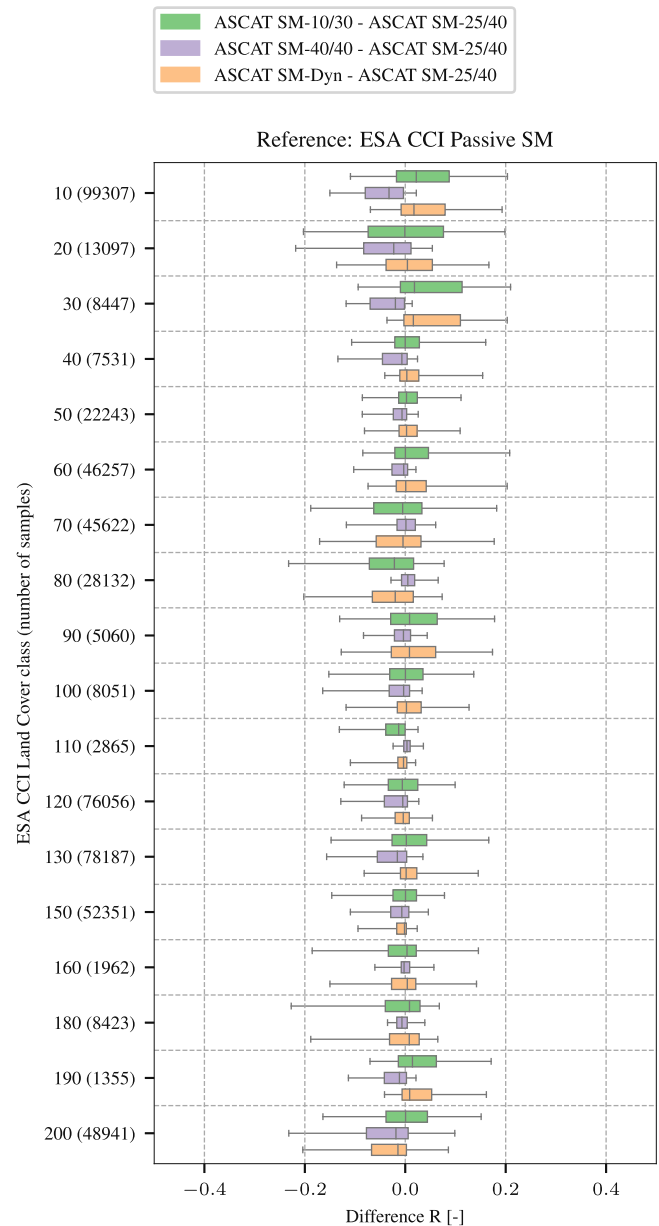


Fig. 10. Difference of Pearson R summarized as boxplot per land cover class using ESA CCI Passive SM as reference. Whisker ends represent 5th and 95th percentile.

puted using ASCAT SM-25/40 and ESA CCI Passive SM [Fig. 8(a)]. However, both cases also indicate strong negative correlations visible in very dry regions (e.g., the Arabian peninsula, North Africa, Namibia, Chile, US Arizona), which has been repeatedly shown by other studies as well [12], [50]–[52]. On-going research suggests that this could be due to subsurface scattering effects with an inverse relationship between backscatter and (low) soil moisture conditions: under very dry soil conditions deeper soil layers might cause volume scattering or scattering by subsurface discontinuities (e.g., bedrock or rocky layer covered by shallow soil), which is entirely obscured during wet soil conditions with an overall lower (surface) scattering intensity [11]. Such an effect has been observed in a field experiment for sandy soils in north-central Florida using an L-band radar instrument [53] and also

reproduced in an indoor laboratory experiment using C-band radar observations [54].

In addition, negative correlations can also be seen in high latitudes ($>65^{\circ}\text{N}$) in the case of GLDAS-2.1 Noah SM [Fig. 7(a)], although not as strong compared to dry environments. In general, northern latitudes present challenging retrieval conditions, especially for coarse resolution instruments such as ASCAT. For example, when frozen soil or snow dominates the instrument footprint, the retrieval of soil moisture is difficult or not possible at all. This is also true for transition periods with snowmelt and (temporary) standing water [55], [56]. However, also the performance of land surface models is restricted in such environments, which, for example, depends on a correct parameterization of snow and frozen soil conditions [57]. Due to these two physical

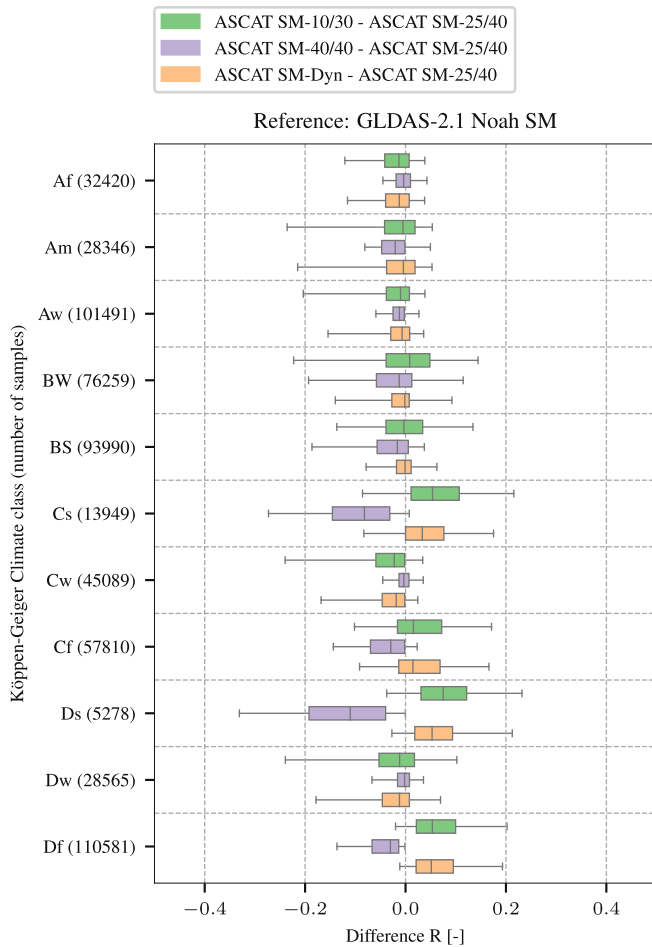


Fig. 11. Difference of Pearson R summarized as boxplot per Köppen Geiger climate class using Noah GLDAS-2.1 SM as reference. Whisker ends represent 5th and 95th percentile.

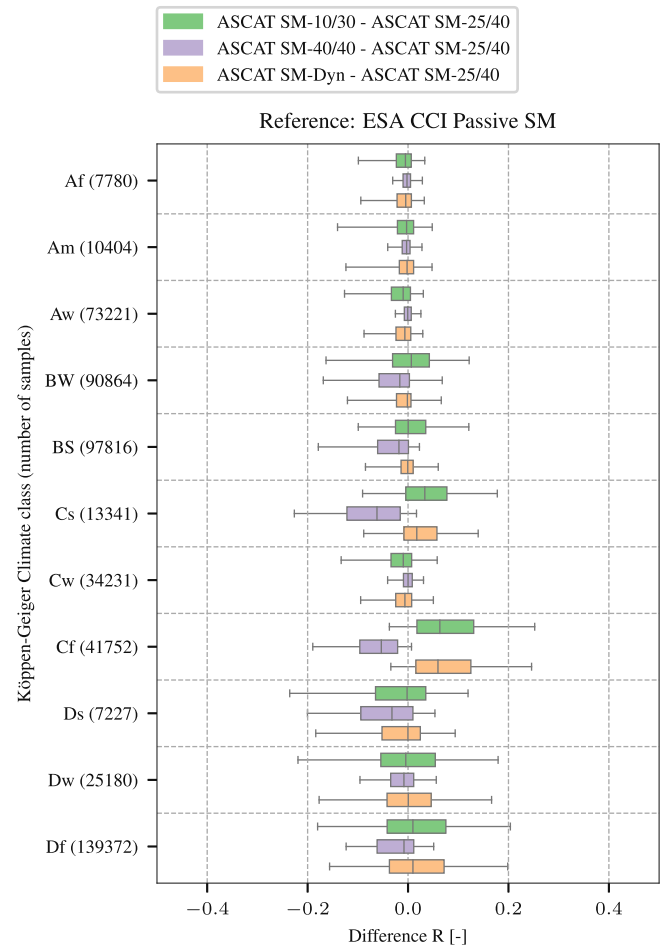


Fig. 12. Difference of Pearson R summarized as boxplot per Köppen Geiger climate class using ESA CCI Passive SM as reference. Whisker ends represent 5th and 95th percentile.

processes leading to negative correlations the differences in R are not shown [Figs. 7(b)–(d) and 8(b)–(d)].

Fig. 7(b) and (c) illustrates the difference of Pearson R between ASCAT SM-25/40 and ASCAT SM-10/30, as well as ASCAT SM-25/40 and ASCAT SM-40/40 using GLDAS-2.1 Noah SM as reference. Positive values indicate improvements with respect to the standard vegetation characterization ($\theta_d = 25^\circ$, $\theta_w = 40^\circ$). North America, Europe, and southern parts of South America show throughout a positive impact of using a stronger vegetation correction [ASCAT SM-10/30, Fig. 7(b)], while a static-only vegetation correction [ASCAT SM-40/40, Fig. 7(c)] leads to an overall lower performance compared to ASCAT SM-25/40. A similar pattern can be seen compared to ESA CCI Passive SM [Fig. 8(b) and (c)] except for some areas in high latitudes, which tend to be better for ASCAT SM-40/40. However, as mentioned before, high latitudes are quite complex environments with an extended cold season leaving not many observations for validation. Poor results using a stronger vegetation correction are clearly visible in parts of Africa and East Asia, as well as India, Bolivia, and Brazil [Figs. 7(b) and 8(b)]. Interestingly, Pearson R tends to be similar between ASCAT SM-25/40 and ASCAT SM-40/40 for exactly these areas [Figs. 7(c) and 8(c)]. A closer examination of these regions

shows that different reasons are causing these unexpected results.

First, semiarid regions, such as the Sahel zone and South Africa, exhibit a high level of variation in their seasonal soil moisture and vegetation dynamics. For example, these areas can suffer from large-scale disruptions, such as fires and subsequent multiannual recoveries. Therefore, the assumption that climatology is able to represent the interannual cycle of vegetation phenology might be insufficient. This was also shown by Vreugdenhil *et al.* [20] who demonstrated that the TUW-SMR soil moisture retrievals improved when using an interannually varying vegetation correction based on VOD from passive microwave observations. More in-depth analysis in South Africa has indicated (not shown) that incorrect (not dry) backscatter observations are selected to determine the dry reference. Hence, a misrepresentation of the interannual vegetation cycle using a climatology of σ' and σ'' is one of the reasons why the lowest backscatter extrapolated to the dry crossover angle no longer corresponds to the driest soil moisture conditions.

Second, the poor performance in India, Bolivia, Brazil, and part of East Asia are related to wetlands. Some of the world's largest wetlands are clearly visible, such as the Amazon River Floodplain, the Pantanal in South America, and

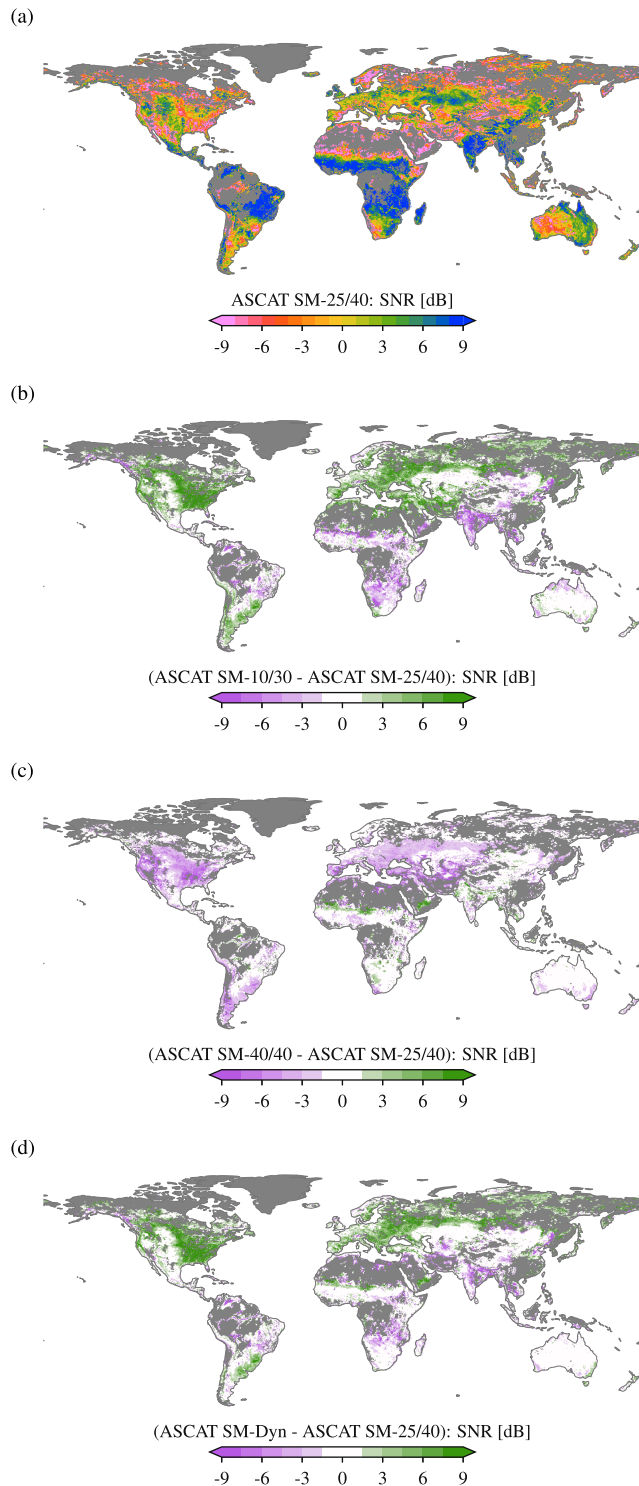


Fig. 13. SNR estimated by TC between ASCAT SM, GLDAS-2.1 Noah SM and CCI Passive SM. Locations only with more than 100 temporally collocated observations and a positive Pearson R between the data sets are shown.

the Sundarbans in the Ganges-Brahmaputra Delta. In Africa, the outline of numerous Zambezi flooded grasslands (e.g., Okavango Delta, Bangweulu Wetlands, and Lukanga Swamp) can be detected. Wetland backscatter signatures are quite unique because the dominant scattering mechanism ranges from surface and volume scattering to specular reflection and

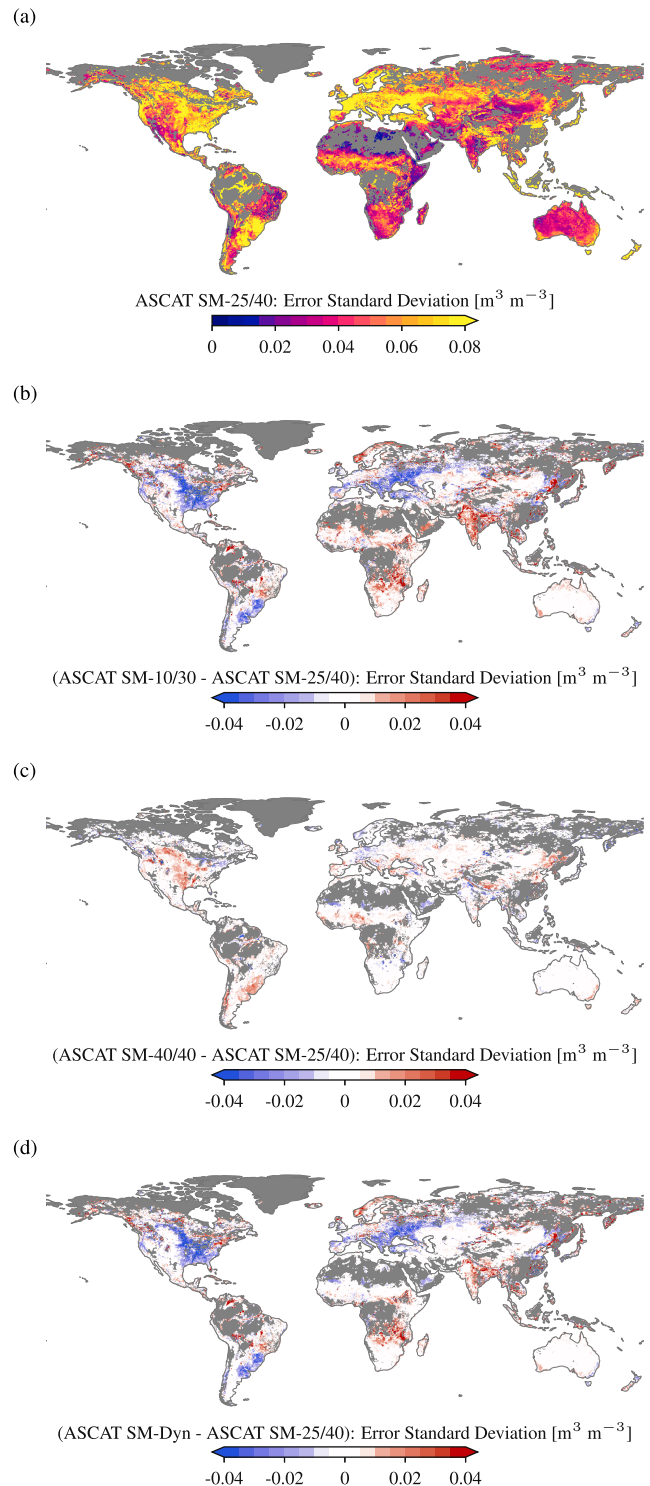


Fig. 14. EStd estimated by TC between ASCAT SM, GLDAS-2.1 Noah SM and CCI Passive SM. Locations only with more than 100 temporally collocated observations and a positive Pearson R between the data sets are shown.

double-bounce effects [58]. Therefore, temporal changes in the incidence angle dependence of backscatter are mainly driven by changes in the scattering mechanism. Further enhancing the vegetation correction may increase already existing errors due to an incorrect representation of the scattering behavior, ultimately misinterpreting vegetation phenology. Similar to

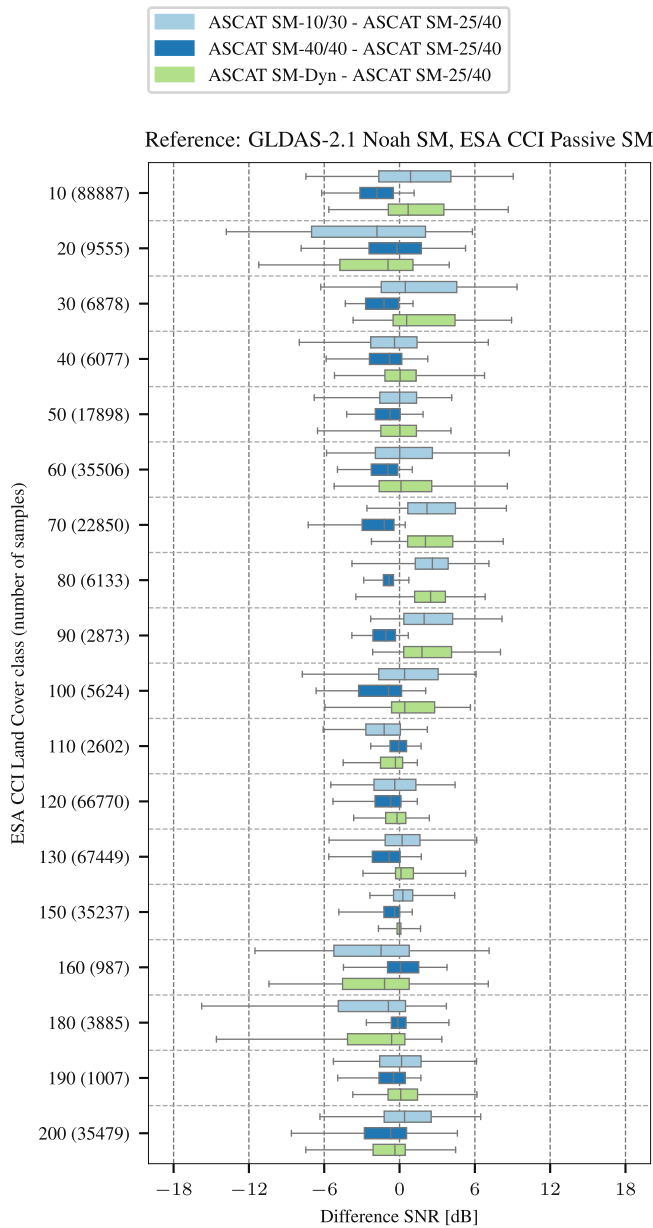


Fig. 15. Difference of SNR summarized as boxplot per land cover class. Whisker ends represent 5th and 95th percentile.

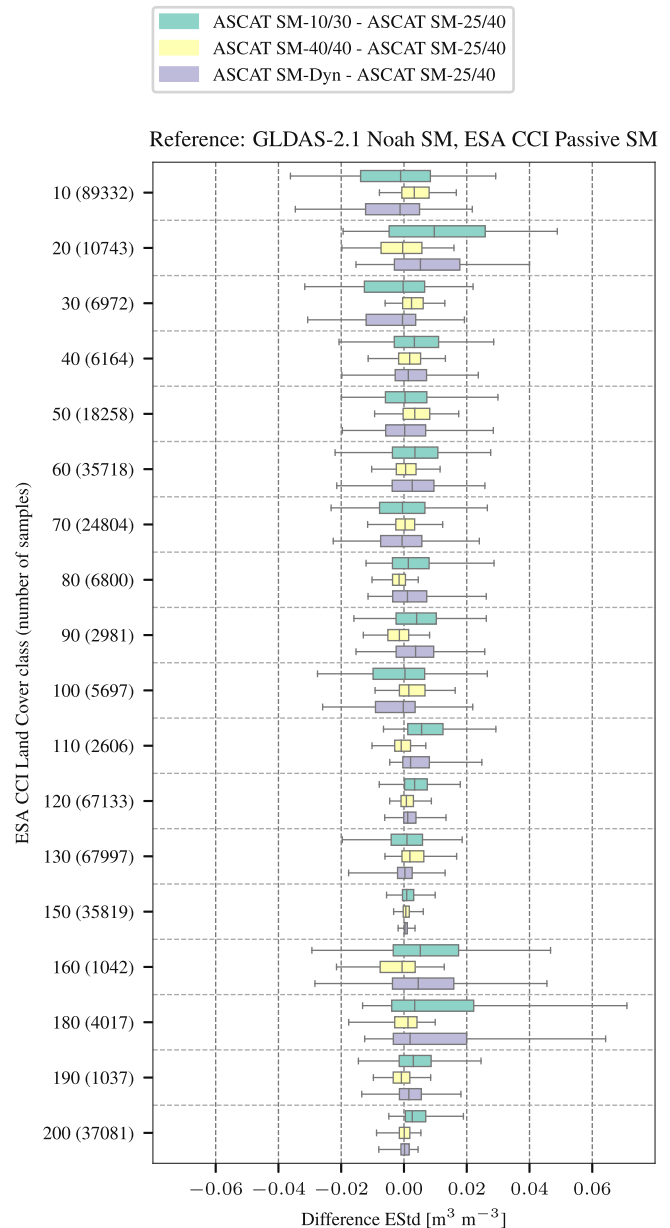


Fig. 16. Difference of EStd summarized as boxplot per land cover class. Whisker ends represent 5th and 95th percentile.

the situation in high latitudes, accurate retrieval of surface soil moisture information is quite complex or impossible in wetlands. Flooding dynamics and vegetation coverage are the main problems. However, Synthetic Aperture Radar (SAR) systems have shown good results mapping and monitoring wetland changes (e.g., [59]), but coarse-scale instruments, such as ASCAT, have a clear handicap.

Finally, a large part of negative Pearson R results using a stronger vegetation correction can be linked to flooded cropland, e.g., visible in Thailand, India, and China. Similar to wetlands, emergent vegetation from continuously or periodically inundated cropland can lead to multiple scattering mechanisms affecting the temporal behavior of σ' and σ'' . In addition, the climatological representation of σ' and σ'' can have a negative impact on both, wetlands and flooded

cropland. As previously mentioned, strong interannual variations can lead to extrapolation errors selecting the wrong backscatter observations for the determination of the dry and wet backscatter reference. In fact, the TUW-SMR has not been developed to model backscatter behavior of flooded vegetation. Therefore, an optimization of the vegetation parameterization will not help in such situations.

Combining the results of Pearson R between ASCAT SM and GLDAS-2.1 Noah SM in CCI Land Cover classes [49] (Fig. 9) and Köppen Geiger climate classes [48] (Fig. 11) shows that tree cover land cover classes (70, 80, 90), as well as cold (Cs, Cf) and temperate (Ds, Df) climates benefit the most from a stronger vegetation correction. Moreover, the performance clearly deteriorates in the case of flooded vegetation (20, 160, 180). The latter is in line with previous

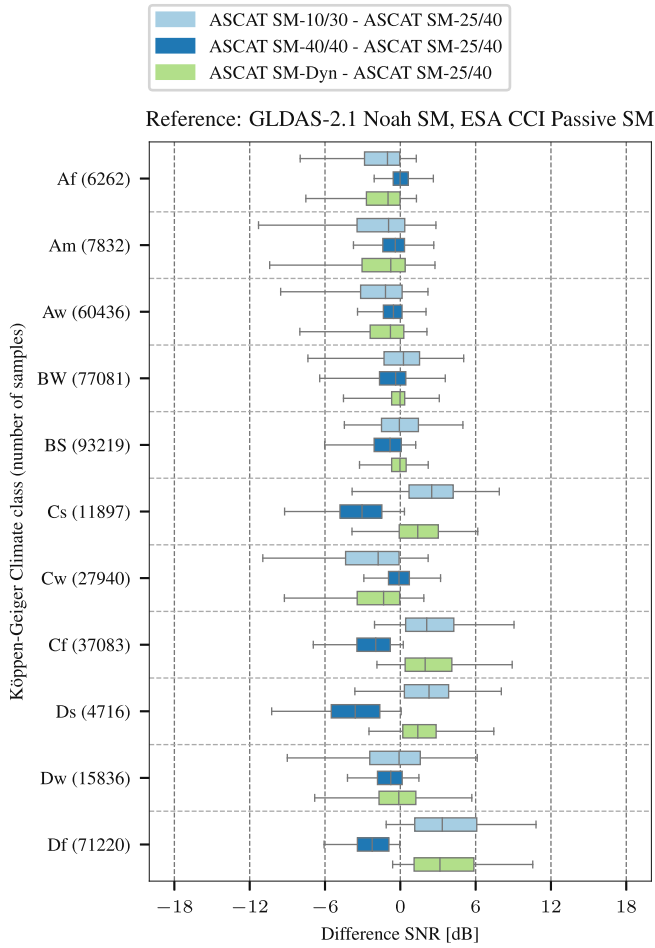


Fig. 17. Difference of SNR summarized as boxplot per Köppen Geiger climate class. Whisker ends represent 5th and 95th percentile.

observations and discussions on mixed scattering behavior in such regions. Interestingly, in some cases the standard vegetation correction seems to be superior, most notably in cropland (20) and shrubland (120).

The performance of ASCAT SM-Dyn is very similar to ASCAT SM-10/30, which is expected because the spatially variable crossover angles are close to $\theta_d = 10^\circ$ and $\theta_w = 30^\circ$ over large parts of the world. The exception is sparsely vegetated and bare areas, where the crossover angles are shifting toward $\theta_d = 40^\circ$ and $\theta_w = 40^\circ$ leading to no seasonal vegetation correction. Therefore, ASCAT SM-Dyn has the advantage of showing good performance in similar areas as ASCAT SM-10/30 compared to ASCAT SM-25/40, while at the same time avoiding an inaccurate and erroneous (seasonal) vegetation correction in areas previously discussed [Fig. 7(d)].

In the case of ASCAT SM and CCI Passive SM (Figs. 10 and 12) the Pearson R results show smaller improvements of ASCAT SM-10/30, illustrating that $\theta_d = 25^\circ$ and $\theta_w = 40^\circ$ have been a good choice on a global basis. However, the performance consistently improves for the cropland classes (10, 20, 30) and cold (Cs, Cf) climates. Similar to GLDAS-2.1 Noah SM, the comparison against ESA CCI Passive SM also shows comparable results between ASCAT SM-Dyn and

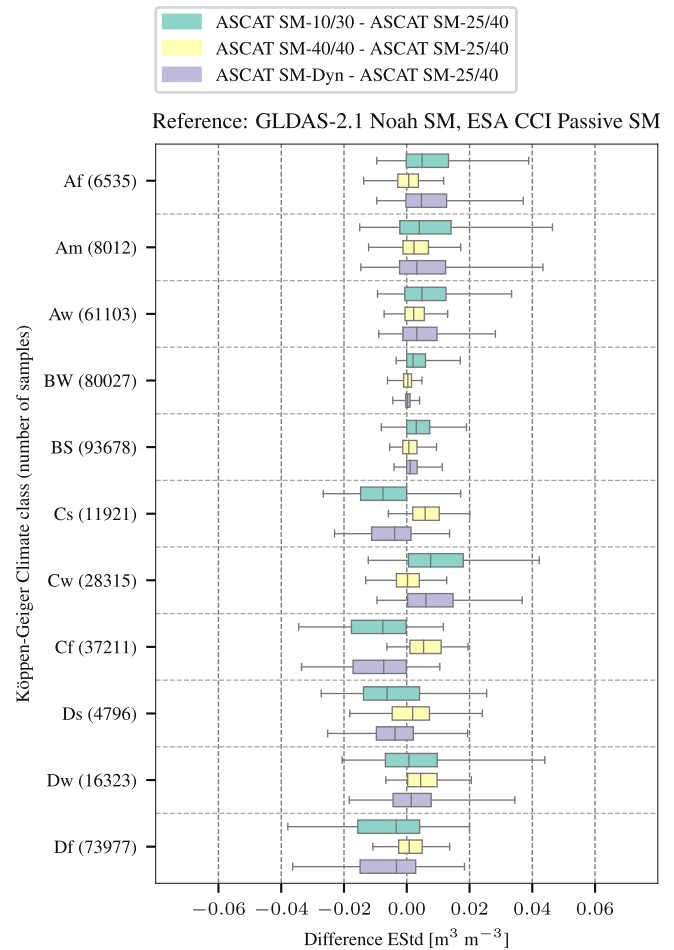


Fig. 18. Difference of EStd summarized as boxplot per Köppen Geiger climate class. Whisker ends represent 5th and 95th percentile.

ASCAT SM-10/30, but again with the same advantage of ASCAT SM-Dyn containing less areas with poor performance.

It has also been tested whether performance differences can be detected computing soil moisture anomalies using a sliding window of five weeks similar to [60]. However, the remaining soil moisture anomaly contains only short term variations and the performance metrics indicate no significant difference for the ASCAT SM data sets (not shown) as the vegetation parameterization affects the seasonality of soil moisture more than short-term changes.

B. Triple Collocation

The error variance computed using TC are presented as SNR in Fig. 13 and scaled error standard deviation (EStd) in Fig. 14. While EStd indicates errors only, SNR presents errors with respect to the signal variance on a logarithmic scale [31].

TC has been applied four times, each time using Noah GLDAS-2.1 SM and CCI Passive SM in combination with a different ASCAT SM data set (see Table III). The results of SNR and EStd are shown in Figs. 13 and 14 only for locations having a positive Pearson R and at least more than 100 temporally collocated soil moisture triplets. The SNR and EStd of ASCAT SM-25/40 [Figs. 13(a) and 14(a)] have

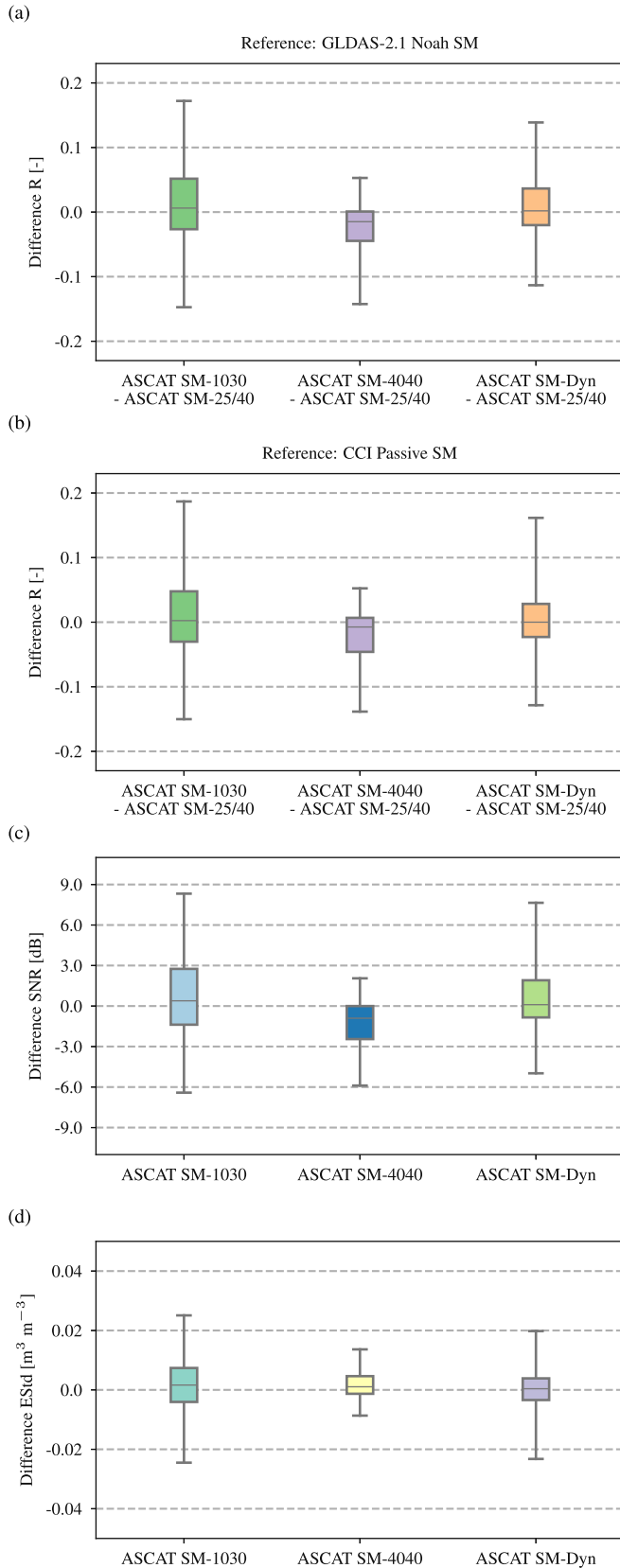


Fig. 19. Difference of Pearson R in case of GLDAS-2.1 Noah SM (a) and CCI Passive SM (b), as well as difference of SNR (c) and EStd (d) summarized as boxplots. Whisker ends represent 5th and 95th percentile.

been used as a baseline and the difference to all other ASCAT SM data sets has been computed.

As can be seen in Fig. 13(b), a stronger vegetation correction (ASCAT SM-10/30) tends to improve SNR especially in the Northern Hemisphere. Many parts of North America and Europe increase from around 0 dB to more than 3–6 dB indicating a substantial improvement in terms of SNR. However, an exceptional decrease of SNR can also be detected, e.g., in India and South Africa dropping more than 3 dB in some parts. As previously discussed in the case of Pearson R , the climatological representation of the vegetation phenology in combination with mixed scattering mechanism is compromising the soil moisture retrieval, which becomes more evident using a stronger vegetation correction (ASCAT SM-10/30). The spatially variable characterization of the crossover angles (ASCAT SM-Dyn) produces more balanced results with less strong negative SNR results [Fig. 13(d)] compared to ASCAT SM-10/30 indicating that a static vegetation correction (like in ASCAT SM-40/40) seems to be the best case scenario at the moment in areas such as Africa and India [Fig. 13(c)] before better characterizing the interannual vegetation cycle. Otherwise, a seasonal vegetation correction has a clear benefit as can be seen in Fig. 13(c) because many areas indicate a negative SNR.

A similar spatial pattern can be found in the case of EStd, representing the scaled EStd. Smaller errors can be found in Eastern Europe and Eastern U.S. for ASCAT SM-10/30 [Fig. 14(b)], as well as countries like Argentina and Uruguay which also benefit from a stronger vegetation correction when compared to ASCAT SM-25/40. As evident in Fig. 14(c), there are no large differences in EStd between ASCAT SM-25/40 and ASCAT SM-40/40. This suggests, that the soil moisture benefits most from applying a seasonal vegetation correction, which becomes even more evident for ASCAT SM-10/30 and ASCAT SM-Dyn.

Like Pearson R , aggregating SNR in terms of CCI Land Cover classes (Fig. 15) and Köpen–Geiger climate classes (Fig. 17) shows better results for tree cover (60, 70, 80, 90, 100) and crop classes (10, 30), as well as cold (Cs, Cf) and temperate climates (Ds, Df). A direct comparison between SNR and EStd suggests that especially tree cover classes (70, 80, 90) gain in terms of signal variance since the median of EStd remains overall close to zero. Looking at areas containing flooded vegetation (20, 160, 180) reveals a higher EStd with an overall reduction of SNR for ASCAT SM-10/30 and ASCAT SM-Dyn, which is consistent with the results based on Pearson R .

VI. CONCLUSION AND OUTLOOK

In this study we investigated the performance of the TUW-SMR using different pairs of dry and wet crossover angles: 1) $\theta_d = 40^\circ$ and $\theta_w = 40^\circ$ which is equivalent to no, respectively, static vegetation correction; 2) $\theta_d = 25^\circ$ and $\theta_w = 40^\circ$ representing the current (standard) seasonal vegetation correction; 3) $\theta_d = 10^\circ$ and $\theta_w = 30^\circ$ describing a stronger seasonal vegetation correction; and 4) a spatially variable choice of crossover angles derived from a VCF data set. A comparison against GLDAS-2.1 Noah SM and ESA CCI Passive SM v04.5 showed that a better performance

in terms of Pearson R and SNR can be achieved using a stronger vegetation correction (ASCAT SM-10/30), which was particularly the case for many parts of North America and Europe. The ASCAT soil moisture data record based on the spatially variable selection of crossover angles (ASCAT SM-Dyn) indicated also a good performance compared to the current seasonal vegetation correction (ASCAT SM-25/40), but with the advantage that over bare or sparsely vegetated land the vegetation correction is switched off. Over vegetated areas, the results of ASCAT SM-40/40 generally showed a lower performance compared to the parameterizations modeling a seasonal vegetation signal (ASCAT SM-25/40, ASCAT SM-10/30, ASCAT SM-Dyn). Hence, these results confirm the value of the information contained in the ASCAT observed slope σ' and curvature σ'' for describing vegetation dynamics [61] and illustrate that it is not enough to just take normalizing backscatter time series for estimating soil moisture as this causes seasonal biases.

The analysis also provided insight into challenging conditions where the TUW-SMR fails to describe all relevant backscatter phenomena, such as subsurface scattering in dry areas or regions with (temporary) flooded vegetation (e.g., wetlands and flooded cropland). Furthermore, we identified a shortcoming related to the climatological characterization of the vegetation cycle. A previous study has tried characterizing σ' and σ'' as time series based on a kernel smoother showing promising results [62], however, further work is needed to combine this method with the new selection of crossover angles investigated in this study. In addition, the assumptions behind the TUW-SMR have been tested and evaluated against a newly developed radiative transfer model (RT1) [63], which has been recently applied to ASCAT [64]. RT1 has shown a very similar functional behavior, but also differences e.g., suggesting a certain dependence between slope and soil moisture. Further research is planned on this subject.

The initial selection of the crossover angles ($\theta_d = 25^\circ$ and $\theta_w = 40^\circ$) has been a robust and effective choice [10], [22], [24], but based on the results presented in this study a stronger vegetation correction helps to improve the ASCAT soil moisture signal [Fig. 13(b) and (d)]. Quantitatively ASCAT SM-10/30 and ASCAT SM-Dyn are showing a similar performance, with less extreme values in the case of ASCAT SM-Dyn (Fig. 19). Apart from that, a spatially variable crossover angle selection is preferable eventually (ASCAT SM-Dyn), because it allows further adjustment of the optimal choice of crossover angles. In fact, some areas still indicate ASCAT SM-25/40 as the best compromise. Therefore, our recommendation for the operational H SAF ASCAT soil moisture data services [11] is to adopt the new spatially variable vegetation parameterization introduced here.

A new generation of C-band scatterometer instrument (called SCA) is currently being prepared and foreseen to be launched in 2024. The SCA instrument will be on-board the Metop Second Generation (Metop-SG) satellite representing the space segment of the EUMETSAT Polar System - Second Generation (EPS-SG). The new Metop-SG constellation will contain three pairs of satellites, i.e., 6 satellites (A1-A3, B1-B3), instead of 3 in the case of Metop (A, B, C). SCA

will be on-board of the B series of the Metop-SG satellites ensuring C-band backscatter measurements until 2040. Apart from an improved radiometric and spatial resolution of SCA compared to ASCAT, a new feature will be an additional VH channel on SCA's Mid beam antennas [65]. This additional source of information can be vital to further optimize and improve vegetation characterization in the TUW-SMR.

REFERENCES

- [1] E. G. Njoku and P. E. O'Neill, "Multifrequency microwave radiometer measurements of soil moisture," *IEEE Trans. Geosci. Remote Sens.*, vol. GE-20, no. 4, pp. 468–475, Oct. 1982.
- [2] T. J. Schmugge, "Remote sensing of soil moisture: Recent advances," *IEEE Trans. Geosci. Remote Sens.*, vol. GE-21, no. 3, pp. 336–344, Jul. 1983.
- [3] E. T. Engman and N. Chauhan, "Status of microwave soil moisture measurements with remote sensing," *Remote Sens. Environ.*, vol. 51, no. 1, pp. 189–198, Jan. 1995.
- [4] M. Owe, R. de Jeu, and J. Walker, "A methodology for surface soil moisture and vegetation optical depth retrieval using the microwave polarization difference index," *IEEE Trans. Geosci. Remote Sens.*, vol. 39, no. 8, pp. 1643–1654, Aug. 2001.
- [5] E. G. Njoku, T. J. Jackson, V. Lakshmi, T. K. Chan, and S. V. Nghiem, "Soil moisture retrieval from AMSR-E," *IEEE Trans. Geosci. Remote Sens.*, vol. 41, no. 2, pp. 215–229, Feb. 2003.
- [6] R. M. Parinussa, T. R. H. Holmes, N. Wanders, W. A. Dorigo, and R. A. M. de Jeu, "A preliminary study toward consistent soil moisture from AMSR2," *J. Hydrometeorology*, vol. 16, no. 2, pp. 932–947, Apr. 2015.
- [7] R. Bindlish, T. Jackson, M. Cosh, T. Zhao, and P. O'Neill, "Global soil moisture from the Aquarius/SAC-D satellite: Description and initial assessment," *IEEE Geosci. Remote Sens. Lett.*, vol. 12, no. 5, pp. 923–927, May 2015.
- [8] Y. H. Kerr *et al.*, "The SMOS mission: New tool for monitoring key elements of the global water cycle," *Proc. IEEE*, vol. 98, no. 5, pp. 666–687, May 2010.
- [9] D. Entekhabi *et al.*, "The soil moisture active passive (SMAP) mission," *Proc. IEEE*, vol. 98, no. 5, pp. 704–716, May 2010.
- [10] W. Wagner, G. Lemoine, and H. Rott, "A method for estimating soil moisture from ERS scatterometer and soil data," *Remote Sens. Environ.*, vol. 70, no. 2, pp. 191–207, Nov. 1999.
- [11] W. Wagner *et al.*, "The ASCAT soil moisture product: A review of its specifications, validation results, and emerging applications," *Meteorologische Zeitschrift*, vol. 22, no. 1, pp. 5–33, Feb. 2013.
- [12] Y. Y. Liu *et al.*, "Developing an improved soil moisture dataset by blending passive and active microwave satellite-based retrievals," *Hydrol. Earth Syst. Sci.*, vol. 15, no. 2, pp. 425–436, Feb. 2011.
- [13] Y. Y. Liu *et al.*, "Trend-preserving blending of passive and active microwave soil moisture retrievals," *Remote Sens. Environ.*, vol. 123, pp. 280–297, Aug. 2012.
- [14] F. T. Ulaby, R. K. Moore, and A. K. Fung, *Microwave Remote Sensing: Active and Passive: Radar Remote Sensing and Surface Scattering and Emission Theory* (Advanced Systems and Applications), vol. 2. Dedham, MA, USA: Artech House, 1986.
- [15] T. J. Jackson and T. J. Schmugge, "Vegetation effects on the microwave emission of soils," *Remote Sens. Environ.*, vol. 36, no. 3, pp. 203–212, Jun. 1991.
- [16] S. Paloscia, G. Macelloni, E. Santi, and T. Koike, "A multifrequency algorithm for the retrieval of soil moisture on a large scale using microwave data from SMMR and SSM/I satellites," *IEEE Trans. Geosci. Remote Sens.*, vol. 39, no. 8, pp. 1655–1661, Aug. 2001.
- [17] J. Kolassa, F. Aires, J. Polcher, C. Prigent, C. Jimenez, and J. M. Pereira, "Soil moisture retrieval from multi-instrument observations: Information content analysis and retrieval methodology," *J. Geophys. Res., Atmos.*, vol. 118, no. 10, pp. 4847–4859, May 2013.
- [18] L. Li *et al.*, "WindSat global soil moisture retrieval and validation," *IEEE Trans. Geosci. Remote Sens.*, vol. 48, no. 5, pp. 2224–2241, May 2010.
- [19] Y. H. Kerr, P. Waldteufel, J.-P. Wigneron, J. Martinuzzi, J. Font, and M. Berger, "Soil moisture retrieval from space: The Soil Moisture and Ocean Salinity (SMOS) mission," *IEEE Trans. Geosci. Remote Sens.*, vol. 39, no. 8, pp. 1729–1735, Aug. 2001.

- [20] M. Vreugdenhil, W. A. Dorigo, W. Wagner, R. A. M. de Jeu, S. Hahn, and M. J. E. van Marle, "Analyzing the vegetation parameterization in the TU-wien ASCAT soil moisture retrieval," *IEEE Trans. Geosci. Remote Sens.*, vol. 54, no. 6, pp. 3513–3531, Jun. 2016.
- [21] Z. Bartalis *et al.*, "Initial soil moisture retrievals from the METOP—A advanced scatterometer (ASCAT)," *Geophys. Res. Lett.*, vol. 34, no. 20, Oct. 2007.
- [22] W. Wagner, J. Noll, M. Borgeaud, and H. Rott, "Monitoring soil moisture over the canadian prairies with the ERS scatterometer," *IEEE Trans. Geosci. Remote Sens.*, vol. 37, no. 1, pp. 206–216, 1999.
- [23] V. Naeimi, K. Scipal, Z. Bartalis, S. Hasenauer, and W. Wagner, "An improved soil moisture retrieval algorithm for ERS and METOP scatterometer observations," *IEEE Trans. Geosci. Remote Sens.*, vol. 47, no. 7, pp. 1999–2013, Jul. 2009.
- [24] W. Wagner, G. Lemoine, M. Borgeaud, and H. Rott, "A study of vegetation cover effects on ERS scatterometer data," *IEEE Trans. Geosci. Remote Sens.*, vol. 37, no. 2, pp. 938–948, Mar. 1999.
- [25] D. J. Leroux *et al.*, "Comparison between SMOS, VUA, ASCAT, and ECMWF soil moisture products over four watersheds in U.S.," *IEEE Trans. Geosci. Remote Sens.*, vol. 52, no. 3, pp. 1562–1571, Mar. 2014.
- [26] W. Wagner *et al.*, "Clarifications on the 'comparison between SMOS, VUA, ASCAT, and ECMWF soil moisture products over four watersheds in U.S.,'" *IEEE Trans. Geosci. Remote Sens.*, vol. 52, no. 3, pp. 1901–1906, Mar. 2013.
- [27] I. Pfeil, M. Vreugdenhil, S. Hahn, W. Wagner, P. Strauss, and G. Blöschl, "Improving the seasonal representation of ASCAT soil moisture and vegetation dynamics in a temperate climate," *Remote Sens.*, vol. 10, no. 11, p. 1788, Nov. 2018.
- [28] M. Rodell *et al.*, "The global land data assimilation system," *Bull. Amer. Meteorol. Soc.*, vol. 85, no. 3, pp. 381–394, 2004.
- [29] W. Dorigo *et al.*, "ESA CCI soil moisture for improved Earth system understanding: State-of-the-art and future directions," *Remote Sens. Environ.*, vol. 203, pp. 185–215, Dec. 2017.
- [30] A. Stoffelen, "Toward the true near-surface wind speed: Error modeling and calibration using triple collocation," *J. Geophys. Res.*, vol. 103, no. C4, p. 7755, 1998.
- [31] A. Gruber, C.-H. Su, S. Zwieback, W. Crow, W. Dorigo, and W. Wagner, "Recent advances in (soil moisture) triple collocation analysis," *Int. J. Appl. Earth Observ. Geoinf.*, vol. 45, pp. 200–211, Mar. 2016.
- [32] Z. Bartalis, K. Scipal, and W. Wagner, "Azimuthal anisotropy of scatterometer measurements over land," *IEEE Trans. Geosci. Remote Sens.*, vol. 44, no. 8, pp. 2083–2092, Aug. 2006.
- [33] V. Naeimi, Z. Bartalis, and W. Wagner, "ASCAT soil moisture: An assessment of the data quality and consistency with the ERS scatterometer heritage," *J. Hydrometeorology*, vol. 10, no. 2, pp. 555–563, Apr. 2009.
- [34] S. Hahn, C. Reimer, M. Vreugdenhil, T. Melzer, and W. Wagner, "Dynamic characterization of the incidence angle dependence of backscatter using metop ASCAT," *IEEE J. Sel. Topics Appl. Earth Observ. Remote Sens.*, vol. 10, no. 5, pp. 2348–2359, May 2017.
- [35] E. P. W. Attema and F. T. Ulaby, "Vegetation modeled as a water cloud," *Radio Sci.*, vol. 13, no. 2, pp. 357–364, Mar. 1978.
- [36] J. Figa-Saldaña, J. J. W. Wilson, E. Attema, R. Gelsthorpe, M. R. Drinkwater, and A. Stoffelen, "The Advanced Scatterometer (ASCAT) on the meteorological operational (MetOp) platform: A follow on for European wind scatterometers," *Can. J. Remote Sens.*, vol. 28, no. 3, pp. 404–412, Jan. 2002.
- [37] R. V. Gelsthorpe, E. Schied, and J. J. W. Wilson, "ASCAT-Metop's advanced scatterometer," *ESA Bull.*, vol. 102, pp. 19–27, May 2000.
- [38] J. J. W. Wilson *et al.*, "Radiometric calibration of the advanced wind scatterometer radar ASCAT carried onboard the METOP—A satellite," *IEEE Trans. Geosci. Remote Sens.*, vol. 48, no. 8, pp. 3236–3255, Aug. 2010.
- [39] C. Anderson *et al.*, "Validation of backscatter measurements from the Advanced scatterometer on MetOp—A," *J. Atmos. Ocean. Technol.*, vol. 29, no. 1, pp. 77–88, Jan. 2012.
- [40] P. Righetti and R. Dyer, "Feasibility of metop—A mission extension on drifting local time," in *Proc. 26th Int. Symp. Space Flight Dyn. (ISSFD)*, Jun. 2017. [Online]. Available: https://issfd.org/ISSFD_2017/Program_2017.html
- [41] M. Rodell, P. R. Houser, A. A. Berg, and J. S. Famiglietti, "Evaluation of 10 methods for initializing a land surface model," *J. Hydrometeorology*, vol. 6, no. 2, pp. 146–155, Apr. 2005.
- [42] H. Beaudoin and M. Rodell, "NASA/GSFC/HSL, GLDAS noah land surface model L4 3 hourly 0.25 × 0.25 degree V2.1, Greenbelt, Maryland, USA, Goddard Earth sciences data and information services center (GES DISC)," 10.5067/E7TYRXPJKWOQ, 2016. Accessed: Mar. 20, 2018.
- [43] A. Gruber, W. A. Dorigo, W. Crow, and W. Wagner, "Triple collocation-based merging of satellite soil moisture retrievals," *IEEE Trans. Geosci. Remote Sens.*, vol. 55, no. 12, pp. 6780–6792, Dec. 2017.
- [44] A. Gruber, T. Scanlon, R. van der Schalie, W. Wagner, and W. Dorigo, "Evolution of the ESA CCI soil moisture climate data records and their underlying merging methodology," *Earth Syst. Sci. Data*, vol. 11, no. 2, pp. 717–739, May 2019.
- [45] *Algorithm Theoretical Baseline Document (ATBD) D2.1 Version 04.5*, ESA CCI Soil Moisture, Eur. Space Agency, ECSAT, U.K., 2019.
- [46] R. van der Schalie *et al.*, "The merging of radiative transfer based surface soil moisture data from SMOS and AMSR-E," *Remote Sens. Environ.*, vol. 189, pp. 180–193, Feb. 2017.
- [47] C. D. M. Hansen, "Measures vegetation continuous fields (VCF) yearly global 0.05 Deg," Nat. Aeronaut. Space Admin., U.S. Government, Tech. Rep. v1, 2018.
- [48] M. C. Peel, B. L. Finlayson, and T. A. McMahon, "Updated world map of the Köppen–Geiger climate classification," *Hydrology Earth Syst. Sci.*, vol. 11, no. 5, pp. 1633–1644, Oct. 2007.
- [49] *Land Cover CCI Product User Guide Version 2.4*, CCI Land Cover, ESA, Paris, France, 2014.
- [50] A. Al-Yaari *et al.*, "Global-scale comparison of passive (SMOS) and active (ASCAT) satellite based microwave soil moisture retrievals with soil moisture simulations (MERRA-Land)," *Remote Sens. Environ.*, vol. 152, pp. 614–626, Sep. 2014.
- [51] F. Fascetti, N. Pierdicca, L. Pulvirenti, R. Crapolicchio, and J. Muñoz-Sabater, "A comparison of ASCAT and SMOS soil moisture retrievals over Europe and Northern Africa from 2010 to 2013," *Int. J. Appl. Earth Observ. Geoinf.*, vol. 45, pp. 135–142, Mar. 2016.
- [52] K. Miyaoka *et al.*, "Triple collocation analysis of soil moisture from Metop—A ASCAT and SMOS against JRA-55 and ERA-interim," *IEEE J. Sel. Topics Appl. Earth Observ. Remote Sens.*, vol. 10, no. 5, pp. 2274–2284, May 2017.
- [53] P.-W. Liu, J. Judge, R. D. DeRoo, A. W. England, T. Bongiovanni, and A. Luke, "Dominant backscattering mechanisms at L-band during dynamic soil moisture conditions for sandy soils," *Remote Sens. Environ.*, vol. 178, pp. 104–112, Jun. 2016.
- [54] K. Morrison and W. Wagner, "Explaining anomalies in SAR and scatterometer soil moisture retrievals from dry soils with subsurface scattering," *IEEE Trans. Geosci. Remote Sens.*, vol. 58, no. 3, pp. 2190–2197, Mar. 2020.
- [55] E. Högström, A. Trofaier, I. Gouttevin, and A. Bartsch, "Assessing seasonal backscatter variations with respect to uncertainties in soil moisture retrieval in Siberian Tundra regions," *Remote Sens.*, vol. 6, no. 9, pp. 8718–8738, Sep. 2014.
- [56] E. Hogstrom and A. Bartsch, "Impact of backscatter variations over water bodies on coarse-scale radar retrieved soil moisture and the potential of correcting with meteorological data," *IEEE Trans. Geosci. Remote Sens.*, vol. 55, no. 1, pp. 3–13, Jan. 2017.
- [57] R. D. Koster, Z. Guo, R. Yang, P. A. Dirmeyer, K. Mitchell, and M. J. Puma, "On the nature of soil moisture in land surface models," *J. Climate*, vol. 22, no. 16, pp. 4322–4335, Aug. 2009.
- [58] S. Schläffer, M. Chini, D. Dettmering, and W. Wagner, "Mapping wetlands in Zambia using seasonal backscatter signatures derived from ENVISAT ASAR time series," *Remote Sens.*, vol. 8, no. 5, p. 402, May 2016.
- [59] F. M. Henderson and A. J. Lewis, "Radar detection of wetland ecosystems: A review," *Int. J. Remote Sens.*, vol. 29, no. 20, pp. 5809–5835, Oct. 2008.
- [60] C. Albergel *et al.*, "Evaluation of remotely sensed and modelled soil moisture products using global ground-based *in situ* observations," *Remote Sens. Environ.*, vol. 118, pp. 215–226, Mar. 2012.
- [61] S. C. Steele-Dunne, S. Hahn, W. Wagner, and M. Vreugdenhil, "Investigating vegetation water dynamics and drought using metop ASCAT over the North American grasslands," *Remote Sens. Environ.*, vol. 224, pp. 219–235, Apr. 2019.
- [62] S. Hahn, C. Reimer, M. Vreugdenhil, T. Melzer, and W. Wagner, "Dynamic characterization of the incidence angle dependence of backscatter using metop ASCAT," *IEEE J. Sel. Topics Appl. Earth Observ. Remote Sens.*, vol. 10, no. 5, pp. 2348–2359, May 2017, doi: 10.1109/jstars.2016.2628523.
- [63] R. Quast and W. Wagner, "Analytical solution for first-order scattering in bistatic radiative transfer interaction problems of layered media," *Appl. Opt.*, vol. 55, no. 20, p. 5379, Jul. 2016.

- [64] R. Quast, C. Albergel, J.-C. Calvet, and W. Wagner, "A generic first-order radiative transfer modelling approach for the inversion of soil and vegetation parameters from scatterometer observations," *Remote Sens.*, vol. 11, no. 3, p. 285, Feb. 2019.
- [65] A. Stoffelen *et al.*, "Scientific developments and the EPS-SG scatterometer," *IEEE J. Sel. Topics Appl. Earth Observ. Remote Sens.*, vol. 10, no. 5, pp. 2086–2097, May 2017.



Sebastian Hahn received the B.Sc. degree in geodesy and geomatic engineering and the M.Sc. degree in geodesy and geophysics from the Vienna University of Technology (TU Vienna), Vienna, Austria, in 2009 and 2011, respectively, where he is pursuing the Ph.D. degree in microwave remote sensing.

He is one of the key developers for the software package Soil Water Retrieval Package (WARP), which represents the implementation of the TU Wien soil moisture retrieval algorithm. He is focused on software development, multiprocessing, model calibration, and algorithmic improvements, which is in light of his Ph.D. studies.

His main research interests include microwave remote sensing over land using active instruments, soil moisture retrieval algorithms, and geophysical validation.



Wolfgang Wagner (Senior Member, IEEE) was born in Austria in 1969. He received the Dipl.-Ing. degree in physics and the Dr.techn. degree in remote sensing from the Vienna University of Technology (TU Vienna), Vienna, Austria, in 1995 and 1999, respectively.

In support of his master's and Ph.D. studies he received fellowships to carry out research at the University of Bern, Atmospheric Environment Service Canada, NASA, ESA, and the EC Joint Research Center. From 1999 to 2001 he was with Deutsches

Zentrum für Luft- und Raumfahrt (DLR). In 2001 he was appointed as a Professor for remote sensing at TU Vienna, where he has been the Head of the Department of Geodesy and Geoinformation since 2012. He is a Co-Founder and the Head of science of the Earth Observation Data Centre for Water Resources Monitoring (EODC). His main research interest is to gain physical understanding of the mechanisms driving the interaction of electromagnetic waves with the land surface. Based on this understanding he has developed models for retrieving soil moisture, biomass, and other land surface variables from scatterometer, SAR and full-waveform lidar observations.

Dr. Wagner is member of the EUMETSAT/ESA Science Advisory Group for Metop-SG SCA. He was a recipient of the International Society for Photogrammetry and Remote Sensing (ISPRS) Frederick J. Doyle Award for his scientific contributions in active remote sensing. Since 2016, he has been the Chair of the Global Climate Observing System (GCOS)/World Climate Research Programme (WCRP) Terrestrial Observation Panel for Climate. From 2008 to 2012 he served as a ISPRS Commission VII President and from 2009 to 2011 as an Editor-in-Chief of the Open Access Journal *Remote Sensing*.



Susan C. Steele-Dunne (Member, IEEE) received the S.M. and Ph.D. degrees in hydrology from the Massachusetts Institute of Technology, Cambridge, MA, USA, in 2002 and 2006, respectively.

She has been with the Faculty of Civil Engineering and Geosciences, Delft University of Technology, Delft, The Netherlands, since 2008. She leads the M-WAVE Group, who perform research from field to global scales, combining *in situ* and spaceborne sensors to improve our understanding of microwave interactions with vegetation. Her research interests

include the use of data assimilation, modeling and machine learning to exploit spaceborne radar instruments for applications in ecosystem and agricultural monitoring.



Mariette Vreugdenhil (Member, IEEE) received the B.Sc. and M.Sc. degrees in Earth sciences with an emphasis on remote sensing from Vrije Universiteit Amsterdam, Amsterdam, The Netherlands, in 2009 and 2011, respectively, and the Ph.D. degree in remote sensing with the Center for Water Resource Systems and Department of Geodesy and Geoinformation, Vienna University of Technology (TU Vienna), Vienna, Austria, in 2016.

She works as a Senior Scientist with the Department of Geodesy and Geoinformation, TU Vienna.

Her research interests are the development of retrieval algorithms for vegetation and soil moisture from active microwave observations, in particular from the advanced scatterometer on-board of EUMETSAT Metop satellites and from the Synthetic Aperture Radars on-board of the Copernicus Sentinel-1 satellites.



Thomas Melzer received the M.Sc. and Ph.D. degrees in computer science from the Vienna University of Technology (TU Vienna), Vienna, Austria, in 1997 and 2002, respectively.

He is with the Institute of Photogrammetry and Remote Sensing (IPF), TU Vienna. His research interests include statistical pattern recognition, object reconstruction from 3-D point clouds, and analysis of scatterometer data.